Petrogenesis of rhyolite-trachyte-basalt composite ignimbrite P1, Gran Canaria, Canary Islands

Armin Freundt and Hans-Ulrich Schmincke

GEOMAR, Forschungszentrum für marine Geowissenschaften, Abteilung Vulkanologie und Petrologie
Kiel, Germany

Abstract. The 14 Ma caldera-forming composite ignimbrite P1 on Gran Canaria (Canary Islands) represents the first voluminous eruption of highly differentiated magmas on top of the basaltic Miocene shield volcano. Compositional zonation of the ignimbrite is the result of vertically changing proportions of four component magmas, which were intensely mixed during eruption: (1) Crystal-poor to highly phyric rhyolite ($\sim$10 km^3), (2) sodic trachyandesite through mafic to evolved trachyte ($\sim$6 km^3), (3) Na-poor trachyandesite ($<$1 km^3), and (4) basalt zoned from 5.2 to 4.3 wt % MgO ($\sim$26 km^3). P1 basalt is composed of two compositionally zoned magma batches, B2 basalt and B3 basalt. B3 basalt is derived from a mantle source depleted in incompatible trace elements compared to the shield basalt source. Basaltic magmas were stored in a reservoir probably underplating the crust, in which zoned B2 basaltic magma formed by mixing of "enriched" (shield) and "depleted" (B3) mafic melts and subsequent crystal fractionation. Evolved magmas formed in a shallow crustal chamber, whereas intermediate magmas formed at both levels. Abundant pyroxenitic to gabbroid cumulates in P1 support crystal fractionation as the major differentiation process. On the basis of major and trace element modeling, we infer two contemporaneous fractional crystallization series: series I from "enriched" shield basalt through Na-poor trachyandesite to rhyolite, and series II from "depleted" P1 basalt through sodic trachyandesite to trachyte. Series II rocks were significantly modified by selective contamination involving feldspar (Na, K, Ba, Eu, Sr), zircon (Zr) and apatite (P, Y, rare earth elements) components; apatite contamination also affected series I Na-poor trachyandesite. Substantial sodium introduction into sodic trachyandesite is the main reason for the different major element evolution of the two series, whereas their different parentage is mainly reflected in the high field strength trace elements. Selective element contamination involved not only rapidly but also slowly diffusing elements as well as different saturation conditions. Contamination processes thus variably involved differential diffusion, partial dissolution of minerals, partial melt migration, and trace mineral incorporation. Magma mixing between trachyte and rhyolite during their simultaneous crystallization in the P1 magma chamber is documented by mutual mineral inclusions but had little effect on the compositional evolution of both magmas. Fe-Ti oxide thermometry yields magmatic temperatures of around 850°C for crystal-poor through crystal-rich rhyolite, $\sim$815°C for trachyte and $\sim$850°–900°C for the trachyandesitic magmas. High 1160°C for the basalt magma suggest its intrusion into the P1 magma chamber only shortly before eruption. The lower temperature for trachyte compared to rhyolite and the strong crustal contamination of trachyte and sodic trachyandesite support their residence along the walls of the vertically and laterally zoned P1 magma chamber. The complex magmatic evolution of P1 reflects the transient state of Gran Canaria's mantle source composition and magma plumbing system during the change from basaltic to silicic volcanism. Our results for P1 characterize processes operating during this important transition, which also occurs on other volcanic ocean islands.

Introduction and Geologic Setting

During the major, Miocene magmatic cycle [*Schmincke*, 1976, 1982, 1990] on the volcanic ocean island of Gran Canaria (28°00′N, 15°35′W) in the Canarian archipelago (east central Atlantic), a major change from basaltic to silicic

volcanism occurred at 14 Ma. The basaltic shield (Miocene Basalt Group, MBG) makes up more than 90% of the volume of the island, but only $\sim$10% is subaerially exposed. The shield is capped by $\sim$300 km^3 of trachytic to peralkaline rhyolitic ignimbrite and lava sheets of the Mogán Group (MG), associated with the central Tejeda caldera. The beginning of silicic volcanism is marked by the compositionally mixed ignimbrite cooling unit P1, which directly overlies shield basalts with no indication for a substantial break in volcanic activity.
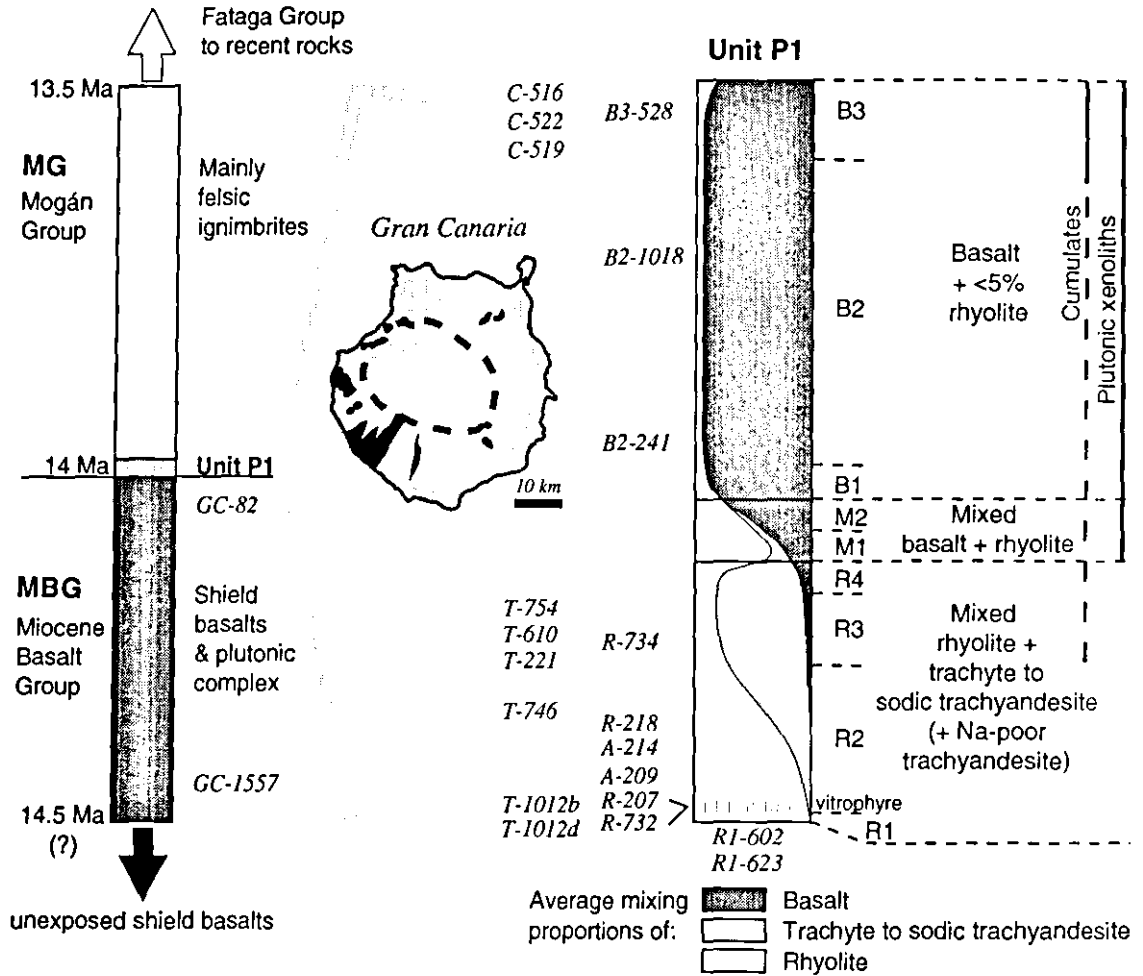
Figure 1. (left) Schematic columnar sections of Miocene Gran Canaria stratigraphy, emphasizing position of P1 at the change from basaltic to silicic volcanism. (right) Ignimbrite P1 subunit stratigraphy and position of key samples. Average mixing proportions of the major component magmas and occurrence of cumulate blocks and plutonic xenoliths are indicated. Inset map shows exposed (black) and reconstructed original distribution (gray) of P1 across the entire island (~45 km diameter) and into the sea; dashed oval outlines Tejeda caldera.

The composite flow P1 is a voluminous (~45 km³), strongly welded ignimbrite sheet which covered the entire island (~45 km diameter) outside the present Tejeda caldera margin with an average thickness of ~30 m. The ignimbrite is composed of four magmatic components, rhyolite, trachyte to sodic trachyandesite, Na-poor trachyandesite, and basalt, which all occur as plastically deformed fiamme and thus were in a liquid state during emplacement. Eruption of P1 probably occurred through a ring fissure system and triggered the initial collapse of the Tejeda caldera. During this eruption the different magma batches mixed in varying proportions, resulting in a deposit zoned from a lower mixed unit containing rhyolite, trachyte, sodic trachyandesite, and subordinate Na-poor trachyandesite, through a central rhyolite-basalt mixed unit to a basaltic unit at the top, which contains only little admixed rhyolite (Figure 1). Abundant gabbro, monzonite, and rare syenite xenoliths and pyroxenitic to gabbroid cumulate fragments occur in the central and top units.

The compositional zonation of the cooling unit is documented in more detail by *Freundt and Schmincke* [1992],

who also described the mixing textures associated with varying component magma proportions and characterized the magma mixing processes. We have shown that a major mixing event involving all component magmas was associated with evacuation of the P1 magma chamber and eruption. The intensity and the systematics of mixing strongly suggest that all component magmas were withdrawn from a single reservoir. Repeated mixing between rhyolitic and trachytic component magmas also occurred during most of their crystallization history prior to eruption, as documented by mutual phenocryst inclusions, implying that both rhyolite and trachyte magmas crystallized in the same reservoir. On the basis of the withdrawal pattern and estimates of the rheological properties of the component magmas, we have then proposed a model of vertical and lateral zonation for the P1 magma chamber at the time of eruption: a core of rhyolite magma, underlain by Na-poor trachyandesite, was mantled by a sheath of vertically zoned trachyte to sodic trachyandesite magma, and basaltic magma intruded into the chamber at the time of eruption.

Here we attempt to reconstruct the petrogenetic processes

Phenocrysts	Rhyolite	Sodic trachy-andesite to trachyte	Sodic trachy-andesite T-754	Na-poor trachy-andesite	Basalt B2 & B3	Pyroxenitic & gabbroid cumulates
Feldspar	Anorthoclase	Oligoclase	Andesine	Andesine	Bytownite	Labradorite
Olivine			●		●	●
Clinopyroxene		●	●	●	●	●
Orthopyroxene		●		●		O
Amphibole	Edenite	Richterite	Kaersutite			O Kaersutite
Biotite	O					
Fe-Ti Oxides	●	●	●	●	●	●
Apatite	●	●	●	●	●	●
Zircon	●					

● present   O rare   high-T [Crystallization Interval] low-T

Figure 2. Phenocryst phases of the P1 component magmas and their relative crystallization intervals (gray) inferred from mutual inclusions. Note that sodic trachyandesite T-754 differs from the other sodic trachyandesite by more calcic feldspar composition, absence of orthopyroxene, and presence of kaersutite, whereas richterite in trachyte to sodic trachyandesite formed very late and mostly occurs in crystalline matrix.

that led to the formation of the component magmas of P1. We will evaluate the intensive parameters of the magma system, discuss chemical variations of the component magmas in terms of the relative importance of crystal fractionation, crustal contamination, and magma mixing prior to eruption, and finally summarize our results in a model outlining the differentiation processes that operated in the magma plumbing system reaching from the mantle source through a deep-seated reservoir up to the shallow P1 magma chamber. Specific problems to be addressed are (1) How did such a diversity of magmas come to reside in the same reservoir? (2) How did the evolved magmas form?

Petrography and Mineralogy

Miocene Basalt Group

Shield basalts on Gran Canaria are mildly alkalic tholeiitic lavas ranging from older picrites to younger hawaiites and mugearites. Mineral assemblages comprise olivine, clinopyroxene, plagioclase, Fe-Ti oxides, and traces of apatite. Plutonic fragments in composite flow P1, derived from an intrusive core of the shield, range from gabbro to syenite, but most are monzonitic with clinopyroxene, plagioclase, Fe-Ti oxides, and apatite; amphibole and olivine are rare. No erupted equivalents of the intermediate to evolved plutonic rocks have been found. Some intermediate to evolved plutonic xenoliths show various degrees of partial melting. Incipient melting is indicated by marginally resorbed plagioclase, whereas major partial melting is indicated by strong resorption of all phases and presence of up to 50% glass, where mingling occurred between partially liquid xenoliths and the host magma.

P1 Component Magmas

Rhyolite is dominated by millimeter-sized anorthoclase crystals (75–92% of the phenocryst fraction). Edenitic amphibole, Fe-Ti oxides, apatite and zircon complete the

mineral assemblage (Figure 2); rare biotite is included in edenite. The rhyolite compositional range is bracketed by three "end-member" varieties: (1) evolved rhyolite (28–37% phenocrysts) with the highest incompatible trace element contents, (2) highly phyric rhyolite (up to 57% crystals), and (3) crystal-poor rhyolite (9–22% phenocrysts) from the poorly welded basal tuff R1 (Figure 1), some of which has a very high silica content due to deuteric silicification of glass shards. Crystal-poor rhyolite is also represented by fiamme and thus is a magmatic component rather than the result of separation of vitric ash and crystals during ash flow transport. Though rare pockets of separated anorthoclase crystals are locally found at the base of the ignimbrite, crystal separation was not efficient to produce a continuous crystal-rich deposit.

Trachyte to sodic trachyandesite contains oligoclase phenocrysts associated with augite, orthopyroxene, Fe-Ti oxides, and apatite as well as late formed richteritic amphibole (Figure 2); the phenocryst content varies from 19 to 37% independent of bulk composition, but the plagioclase/pyroxene ratio and oligoclase crystal size increase with silica content. One inclusion of sodic trachyandesite (sample T-754) contains more calcic plagioclase and kaersutitic amphibole together with augite; orthopyroxene is absent and olivine is rare. Data presented below suggest that this sample represents magma formed at greater depth than the other sodic trachyandesite.

Na-poor trachyandesite is a volumetrically subordinate component of P1. The mineral assemblage comprises plagioclase, augite, orthopyroxene, Fe-Ti oxides, and apatite.

P1 basalt is almost aphyric with <2% plagioclase, clinopyroxene, Fe-Ti oxides, olivine (iddingsitized), and apatite. The olivine content increases upward through the basaltic unit. As discussed below, we distinguish B2 basalt and B3 basalt by their distinct chemical compositions. Both types are compositionally zoned. B2 basalt makes up subunits B1
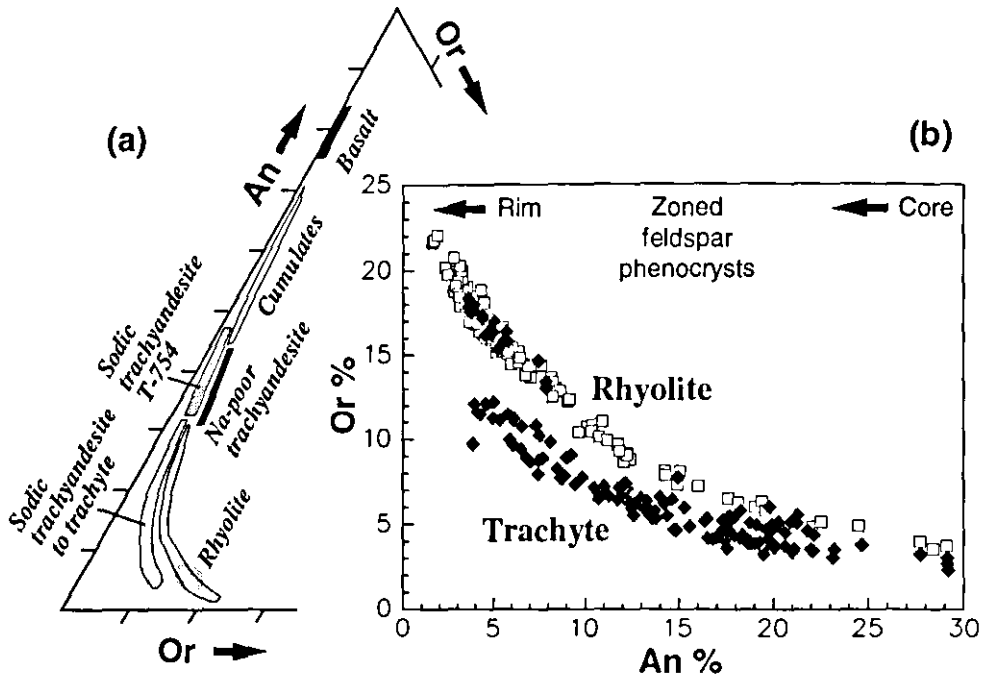
Figure 3. (a) Compositional fields of feldspar phenocrysts in P1 component rocks. The white field for rhyolite includes zoned crystals, and the gray oval denotes only unzoned anorthoclase. Note higher Or solid solution in Na-poor trachyandesite compared to sodic trachyandesite. (b) Composition of zoned crystals from rhyolite and trachyte. Individual compositional zones in trachyte phenocrysts plot into the rhyolite field, mainly at around 5 and 20% An.

and B2, and B3 basalt is largely confined to subunit B3 (Figure 1), but there is no sharp compositional boundary.

Most of the cumulates are gabbroid with parageneses of plagioclase, clinopyroxene, Fe-Ti oxides, olivine, apatite, and rare orthopyroxene; pyroxenitic cumulates contain clinopyroxene, olivine, Fe-Ti oxides, plagioclase, apatite, and rare kaersutite. Clinopyroxene megacrysts (up to 7 cm long) also occur in the basalt and, like the cumulates, do not show any reaction with their host magma.

The sequence of crystallization of the P1 component magmas as inferred from mutual mineral inclusions is shown in Figure 2. The order of crystallization of olivine, clinopyroxene, and plagioclase in P1 basalt cannot be determined, but plagioclase always formed later than the ferromagnesian minerals in the cumulates.

Phenocryst Compositions

Mineral and glass spot analyses were performed on a wavelength-dispersive electron microprobe (CAMEBAX) with 15 kV, 14–15 nA, 10 s counting time, and defocused beam.

Feldspar. Phenocrysts (An_{83-76}) in P1 basalt are more calcic than plagioclase crystals in the various cumulates (An_{71-44}). Interstitial plagioclase of low anorthite content (An_{56-50}) in pyroxenitic cumulates suggests delayed plagioclase precipitation under high P_{H_2O}. Andesine compositions of Na-poor trachyandesite (An_{43-31}) overlap with those of phenocrysts from sodic trachyandesite T-754 (An_{47-34}). However, Na-poor trachyandesite phenocrysts have higher Or contents (Or_{5-3}) than those of T-754 (Or_{3-1}) even though the bulk rock K/Na ratio is lower. Since Or solid solution increases toward lower P_{H_2O} [Brown, 1993], the clinopyroxene-bearing Na-poor trachyandesite magma crystallized un-

der significantly lower water pressure than the amphibole-bearing T-754 magma. The low-Or plagioclase trend of T-754 extends toward the low-Or oligoclase field of trachyte to sodic trachyandesite (Figure 3). Oligoclase phenocrysts of the sodic trachyandesite-trachyte series form a tightly defined trend (An_{32-6}). Feldspar compositions from sodic trachyandesite through evolved trachyte overlap completely, many crystals being strongly zoned over the entire compositional range (Figure 3). Moreover, oligoclase composition in one K_2O-rich trachyte sample (T-1012b) is identical to that in sodic trachyte. Most anorthoclase phenocrysts of P1 rhyolite are homogeneous or weakly zoned (An_{1-8}, Or_{13-22}). Phenocrysts from evolved, highly phyric or crystal-poor rhyolite do not differ in composition. About 20% of the phenocrysts are, however, strongly zoned from anorthoclase rims to oligoclase cores (up to An_{31}, Or_4). Zoned phenocrysts of the rhyolite define a continuous trend at elevated Or contents compared to zoned oligoclase crystals from the trachyte (Figure 3). Individual zones within trachyte phenocrysts plot away from the main trachyte compositional field and fall into the rhyolite field. Such zones mainly occur at the high- and low-An ends of the trachyte field and document mixing events of trachyte with rhyolite. The melt around these crystals thus periodically attained a rhyolite-dominated composition but later changed back to trachyte composition.

Amphibole. Low-Al (<0.5 per formula unit) richteritic amphibole of P1 trachyte is largely confined to the matrix but also occurs in glassy rocks where it formed as a very late phenocryst phase. Edenite phenocrysts of the rhyolite span an intermediate range of Al contents (0.8–1.3 per formula unit). Phenocrysts of T-754 and interstitial amphibole in pyroxenitic cumulate C-251 have kaersutitic compositions

rich in Al (around 1.8 per formula unit) and Ti (around 0.5 per formula unit).

Pyroxene. Orthopyroxenes in sodic trachyandesite to trachyte and in a gabbroid cumulate (C-516) have almost identical compositions, whereas orthopyroxene in Na-poor trachyandesite is slightly more Fe-rich; the corresponding clinopyroxenes show the reverse behavior. Clinopyroxenes can be divided into a high Al/Ti = 3–4 group comprising basalt, sodic trachyandesite T-754, and the cumulates and a low Al/Ti < 3 group comprising Na-poor trachyandesite and sodic trachyandesite to trachyte. There is a tendency for clinopyroxene phenocrysts to become more Fe-rich from sodic trachyandesite to evolved trachyte, but the whole compositional range can be found within a single specimen.

Fe-Ti oxides. All P1 rocks contain both spinel- and rhombohedral-phase Fe-Ti oxides. Both oxide phases are Mg-, V-, and Al-rich in the mafic rocks but increasingly Mn-rich in the evolved rocks. Sodic trachyandesite to trachyte oxides are highly variable in composition ($0 < X_{usp} < 0.8$, $0.77 < X_{ilm} < 0.96$) but without systematic changes across this compositional range. Oxides in the rhyolite, on the other hand, are compositionally well defined ($0 < X_{usp} < 0.35$, $0.82 < X_{ilm} < 0.85$). Cumulate oxides can be divided into an early formed group of euhedral crystals and inclusions in other minerals and a late formed group of anhedral interstitial crystals. Magnetites from both groups do not significantly differ in composition, but late formed ilmenites ($0.89 < X_{ilm} < 0.94$) are clearly distinct from early formed crystals ($0.79 < X_{ilm} < 0.86$).

Thermobarometric Constraints

Thermometric Methods

Fe-Ti oxide thermometry and oxygen barometry. Thermometric calculations were performed with a program (kindly supplied by J. C. Stormer in 1986) following the recalculation scheme of *Stormer* [1983]. The T-f_{O_2} calculations after *Spencer and Lindsley* [1981] use thermodynamic parameters from D. H. Lindsley, which supersede those of *Andersen and Lindsley* [1985]. Equilibrium between selected Fe-Ti oxide pairs was checked petrographically, by electron backscatter imaging, and by Mg/Mn partitioning after *Bacon and Hirschmann* [1988].

Ilmenite-pyroxene thermometry. Temperature calculations are based on the exchange of Mg and Fe^{2+} between ilmenite and orthopyroxene or clinopyroxene after *Bishop* [1980] and are insensitive to pressure ($5°/100$ MPa); all our results refer to 200 MPa. We only used pyroxenes with almost quadrilateral composition (80–95 mol % in clinopyroxene, >95 mol % in orthopyroxene), in agreement with Bishop's database.

Two-pyroxene thermometry. Calculation procedures from *Nielsen and Drake* [1979] and *Brey and Köhler* [1990] were employed to calculate equilibrium temperatures from two-pyroxene assemblages. The *Nielsen and Drake* [1979, equation (39)] approach is based on a data set largely from lunar basalts at 1 atm and $1100°–1350°C$. The Brey and Köhler thermometer, based on natural four-phase lherzolite under $P = 1–6$ GPa and $T = 900°–1400°C$, shows a pressure dependence of $4°/100$ MPa in the range considered here; our results are for 200 MPa. Neither database comprises rock compositions similar to those studied here.
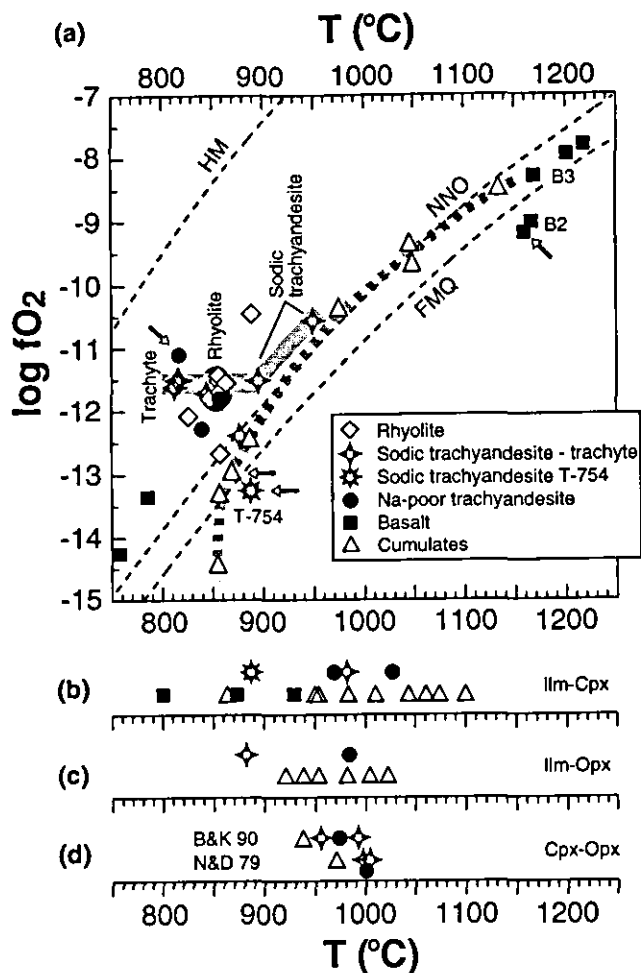

Figure 4. (a) T-f_{O_2} data calculated from coexisting Fe-Ti oxides as explained in the text. Small arrows indicate oxide pairs which petrographically do not show disequilibrium but are outside Mg/Mn equilibrium [after *Bacon and Hirschmann*, 1988]. Note that trachyte is oxidized with respect to sodic trachyandesite, and B3 basalt is slightly more oxidized than B2 basalt. Cumulate data define a high- (along NNO) and a low-temperature group (near FMQ) of early and late formed crystals. Buffer curves calculated after *Wones* [1982]. (b) Ilmenite-clinopyroxene and (c) ilmenite-orthopyroxene temperatures calculated after *Bishop* [1980]. (d) Two-pyroxene temperatures based on average mineral compositions, calculated after *Brey and Köhler* [1990] (B&K 90) and *Nielsen and Drake* [1979] (N&D 79).

Magmatic Temperatures

Results of the temperature calculations are summarized in Figure 4. Temperatures estimated from Fe-Ti oxides probably record magmatic temperatures just prior to eruption because the oxide minerals equilibrate rapidly with changing melt conditions [*Buddington and Lindsley*, 1964; *Haggerty*, 1976]. Higher temperatures estimated from two-pyroxene assemblages are thus consistent with oxide-based temperatures. Ilmenite-pyroxene temperatures mostly overlap with Fe-Ti oxide- and pyroxene-based temperatures. Fe-Ti oxide temperatures for P1 rhyolite cluster around 850°C, which agrees with 848°C from Fe-Ti oxides and 851°C from feldspar-magnetite oxygen isotope fractionation determined by *Crisp and Spera* [1987] on a P1 rhyolite sample. Sodic

trachyandesitic rocks including T-754 yield 950°C to 878°C. Pl trachyte, with temperatures of 813°–845°C (slightly below Pl rhyolite), is more strongly oxidized than sodic trachyandesite, which may reflect introduction of water or loss of hydrogen (Figure 4). Na-poor trachyandesite shows low Fe-Ti oxide temperatures of 817°–857°C, whereas pyroxene-based temperatures are similar to those for sodic trachyandesite (Figure 4). Data for Pl basalt define a high-temperature phenocryst group (1160°–1219°C), where B3 basalt is slightly hotter and more oxidized than B2 basalt, and a low-temperature matrix group (757°–786°C). Early and late formed Fe-Ti oxides in the pyroxenitic and gabbroic cumulates, as distinguished in the previous section, form a high-temperature group at 1135°–975°C and a low-temperature group at 887°–855°C with reduced f_{O_2} (Figure 4).

In summary, Fe-Ti oxide results suggest a temperature gradient in the Pl magma chamber before eruption which ranged from ~815°C (trachyte) through 850°C (rhyolite) to >880°C (trachyandesite). Preservation of a high-temperature (~1160°C) record in the mineral compositions and the crystal-poor nature of Pl basalt suggest that this melt intruded into the Pl reservoir only at the time of eruption so that it was not significantly cooled by the resident evolved magmas. Since Fe-Ti oxide-based temperatures are rather constant for evolved rhyolite, highly phyric rhyolite, and crystal-poor rhyolite, which probably represent different sites in the reservoir, there is no indication of a substantial temperature gradient within the 10 km^3 volume of erupted rhyolite.

Crystallization Pressures and Water Contents

Experiments by *Fisk et al.* [1988] on Reunion basalts, compositionally similar to the Miocene Gran Canaria basalts, show that (1) plagioclase-free, olivine-clinopyroxene-oxide-phyric shield picrites fractionated at >400–600 MPa pressure, and (2) the crystallization sequence olivine-clinopyroxene-plagioclase of the mafic cumulates (which we also infer for the more evolved basalts including Pl basalt) is only realized at >300–400 MPa. On the basis of basaltic plagioclase-saturated compositions, *Grove et al.* [1989] derived an empirical barometer using Al^{VI} in augite. Pressures calculated from clinopyroxenes containing Al^{VI} are 480 to 510 ± 100 MPa for pyroxenitic and gabbroid cumulates (42% of analyzed clinopyroxenes contain Al^{VI}), 680 ± 100 MPa for clinopyroxene megacrysts (63%), 530 ± 150 MPa for Pl basalt (33%), 420 ± 100 MPa for amphibole-bearing sodic trachyandesite T-754 (72%), and 340 ± 150 MPa for sodic trachyandesite to trachyte (43%). Only 13% of the clinopyroxenes in Na-poor trachyandesite contain Al^{VI}; this magma thus crystallized under low pressure. Clinopyroxenes yielding >400 MPa pressure all belong to the high Al/Ti > 3 compositional group. For similar melt compositions, such as T-754 and the other trachyandesites, higher Al/Ti clinopyroxenes reflect higher crystallization pressure as shown by the experiments of *Akella and Boyd* [1973]. Comparison with experiments on andesitic compositions by *Stern et al.* [1975] suggests a pressure >400 MPa for sodic trachyandesite T-754 to realize the crystallization sequence clinopyroxene-amphibole-plagioclase. *Blundy and Holland* [1990] provided a thermobarometric expression based on the amphibole-plagioclase exchange (Ed + 4Qz = Tr + Ab), which yields strongly pressure-dependent temperatures (about −16°C/100 MPa). Comparison of their expression with the temperature ranges obtained from Fe-Ti oxide thermometry suggests pressures of 200–600 MPa for amphibole-bearing

sodic trachyandesite T-754 and ~900 MPa for amphibole-bearing pyroxenitic cumulate C-251. The maximum temperature of 800°C (at $P = 0$) obtained from their expression for Pl rhyolite fails to reach the 850°C oxide temperature, which may be taken to indicate very low pressure. It should be noted, however, that the Blundy and Holland formulation is subject to considerable debate [*Hammarstrom and Zen*, 1992; *Rutherford and Johnson*, 1992; *Poli and Schmidt*, 1992; *Blundy and Holland*, 1992a, b]. The almost total overlap of amphibole and oligoclase/anorthoclase crystallization in Pl rhyolite (Figure 2) suggests crystallization close to the crossing of the respective liquidi, which would be under low pressure of ~100–300 MPa and at H$_2$O > 4 wt % when compared to experiments on calc-alkaline rhyolites [*Naney*, 1983]. The water content of Pl basalt calculated from plagioclase-melt equilibrium after *Housh and Luhr* [1991] is 2–3 wt % H$_2$O (average plagioclase composition, bulk rock as melt composition, $T = 1160$°C, $P = 500$ MPa, but there is no significant pressure dependance). None of the more evolved rocks gave equilibrium results with this method. Since Pl intermediate magmas had pyroxene rather than plagioclase as the liquidus phase, a water content of at least 2 wt % (for $P < 1$ GPa) is suggested from comparison with the experimental results of *Stern et al.* [1975]. As discussed above, higher Or solid solution in plagioclase of Na-poor trachyandesite indicates lower water content of this magma compared to sodic trachyandesite T-754.

In summary, the basaltic magmas probably differentiated at pressures of about 400–500 MPa. This pressure level coincides with the depth of the Moho (14–15 km) underneath Gran Canaria [*Banda et al.*, 1981], suggesting that basaltic magmas ponded in a reservoir at the base of the crust. Amphibole-bearing sodic trachyandesite T-754 also appears to have crystallized at this level. The other intermediate and evolved magmas of Pl crystallized at a shallow level within the crust. With H$_2$O ≥ 4 wt %, Pl rhyolite and trachyte would have reached water saturation at a depth corresponding to $P ≥ 100$ MPa. Bubble wall shards in poorly welded Pl tuff show that oversaturation was reached at the time of eruption; the Pl magma chamber thus probably resided at a level of 100–200 MPa.

Major and Trace Element Variations

Analytical Details

We have preferentially analyzed fiamme but also have used some glassy or dense bulk tuff samples as representatives of magmatic end-members of the composite flow Pl. Neither modal analyses nor extensive detailed field mapping produced evidence that bulk tuff composition is significantly perturbed by fractionation of crystals and vitric ash during transport. Key samples are shown in Figure 1, and their analyses are available as electronic supplement.[1] Chemical

---

[1] An electronic supplement of this material may be obtained on a diskette or Anonymous FTP from KOSMOS.AGU.ORG. (LOGIN to AGU's FTP account using ANONYMOUS as the username and GUEST as the password. Go to the right directory by typing CD APEND. Type LS to see what files are available. Type GET and the name of the file to get it. Finally, type EXIT to leave the system.) (Paper number 94JB02478, Petrogenesis of rhyolite-trachyte-basalt composite ignimbrite Pl, Gran Canaria, Canary Islands, by A. Freundt and H.-U. Schmincke). Diskette may be ordered from American Geophysical Union, 2000 Florida Avenue, N.W., Washington, DC 20009; $15.00. Payment must accompany order.

analyses of major and trace elements were obtained by X ray fluorescence (XRF) analysis of glass pellets with a Phillips PW 1400. Fe^{2+}, CO_2, and H_2O were determined by titration methods. Inductive neutron activation analyses (INAA) of selected trace and rare earth elements (REE) were performed by J. Hertogen, Katholieke Universiteit Leuven, Belgium. Chemical data are recalculated as H_2O-free, and appropriate CaO to combine with CO_2 to make $CaCO_3$ was subtracted from determined CaO. Rock names refer to the total alkalies-silica (TAS) nomenclature after *Le Maitre et al.* [1989]. Mafic rocks are silica-saturated with little normative quartz (qz <5%) but silica oversaturation increases to more evolved compositions, reaching up to 43% normative qz in rhyolite.

Chemical Variations

We include the Miocene shield basalts and the plutonic rocks in the chemical variation diagrams because these are potential parental compositions of the P1 magmas. The entire suite of rocks shows a decrease in FeO, MgO, and CaO and the ferromagnesian trace elements Ni, Cr, V, Sc, and Co from mafic to evolved rocks (Figure 5), reflecting olivine and pyroxene fractionation. TiO_2, P_2O_5, Al_2O_3, and Sr are enriched toward higher silica content in the mafic range but drop at $SiO_2 > \sim 50$ wt %, marking the beginning of substantial Fe-Ti oxide, apatite, and plagioclase fractionation. K_2O and Na_2O are continuously enriched toward higher silica content, sodic trachyandesite to trachyte being more sodic and less potassic than the other rocks (Figure 5). Incompatible elements such as Zr, Nb, Hf, and Th are strongly enriched in the evolved rocks (2–3x basalt). The evolution of REE patterns from mafic to evolved rocks is compatible with fractionation of observed pyroxenitic to gabbroid cumulates. These are composed of the appropriate olivine-clinopyroxene-plagioclase-oxide-apatite mineral assemblages and have REE distributions dominated by clinopyroxene (Figures 6a and 6b). Fractional crystallization thus seems to be the major process of differentiation.

All P1 rocks cannot, however, be related by a single fractionation sequence, because sodic trachyandesite to trachyte follows paths in K_2O, Na_2O (Figure 5), and many trace element diagrams (Figure 7) that are separate from the other rocks. Moreover, a number of rocks clearly deviate from the chemical variations that would be expected from fractional crystallization:

1. P1 basalt differs from shield basalts of similar silica content, clearly showing higher P_2O_5, Al_2O_3, Na_2O, Sr, FeO, and MnO contents and lower MgO, CaO, Cr, Ni, Co, Zr, and Nb concentrations (Figures 5 and 7a–7c). P1 basalt also has a small positive Eu anomaly (Figures 6b and 7c).

2. Unusually high P_2O_5 concentrations, which are clearly incompatible with fractionation of apatite-rich cumulates (such as C-242 in Figure 7b), are also observed in the two Na-poor trachyandesite samples (A-209, A-214), in two rhyolite and trachyte samples, and in some plutonic xenoliths. These rocks are also enriched in Y and the middle REE. A partially molten plutonic xenolith (X-815) with very high P_2O_5 content (corresponding to ~21 wt % apatite) would be an appropriate crustal contaminant to cause excess P enrichment of magma batches.

3. The Zr/Nb ratio remains approximately constant at a typical Mogán Group value of ~6 [*Schmincke*, 1990, Figure 7d] for all rocks except sodic trachyandesite to trachyte,

through which Zr/Nb increases. The sodic trachyandesite to trachyte series is also strongly enriched in Ba, whereas the other rocks follow a trend of moderate Ba enrichment (Figure 7a). Additionally, sodic trachyandesite has a very large positive Eu anomaly (Figure 7c); the size of the Eu anomaly diminishes toward evolved trachyte while REE concentrations increase with silica content (Figure 6d). The REE composition of sodic trachyandesite T-754 is similar to the other sodic trachyandesite except for a less well developed positive Eu anomaly. All sodic trachyandesite to trachyte rocks are Na-rich, except for one sample which is K-rich (T-1012b, Figure 5).

4. In P1 rhyolite, incompatible elements such as Y, Zr, Nb, and the REE decrease in concentration from evolved to highly phyric and high-silica crystal-poor rhyolite (Figures 7b and 7d). The composition of crystal-poor rhyolite does not approach matrix glass composition, as would be expected from anorthoclase-dominated fractionation (Figures 7c and 6c).

Models of Magma Formation

Here we will consider the importance of fractional crystallization, crust/mantle melting, and magma mixing for each of the P1 component magmas with proper attention to the deviations noted above.

Model Calculation Methods

We have determined possible cumulate/restite fractions and compositions relating mafic and evolved magmas by least squares mass balance calculations for major elements (Table 1). In some mass balance calculations, large errors for K_2O or P_2O_5 caused a high residual >1 which improved to <1 when this element was omitted. Trace element calculations involve mineral melt partition coefficients taken from mineral, glass, and rock analyses and from the literature (a table of partition coefficients is available as electronic supplement). The following trace element calculations were performed:

Batch melting

$$C_L = C_0[F + D - (FD)]^{-1} \qquad (1)$$

Rayleigh fractionation

$$C_L = C_0 F^{(D-1)} \qquad (2)$$

C_L is the element concentration in daughter melt, C_0 is the element concentration in parent melt, F is the residual melt fraction, and D is the bulk distribution coefficient. Rayleigh fractionation assumes instantaneous separation of solids and liquid and seems to be mostly applicable to low-viscosity magmas. For high-viscosity magmas, experimental and theoretical work suggests that the major fractionation process is crystallization along magma chamber walls and extraction of residual melt to be mixed with the interior magma [e.g., *McBirney*, 1980; *Sparks et al.*, 1984; *Tait et al.*, 1989]. An appropriate trace element fractionation formulation has been derived by *Langmuir* [1989]:

In situ crystallization
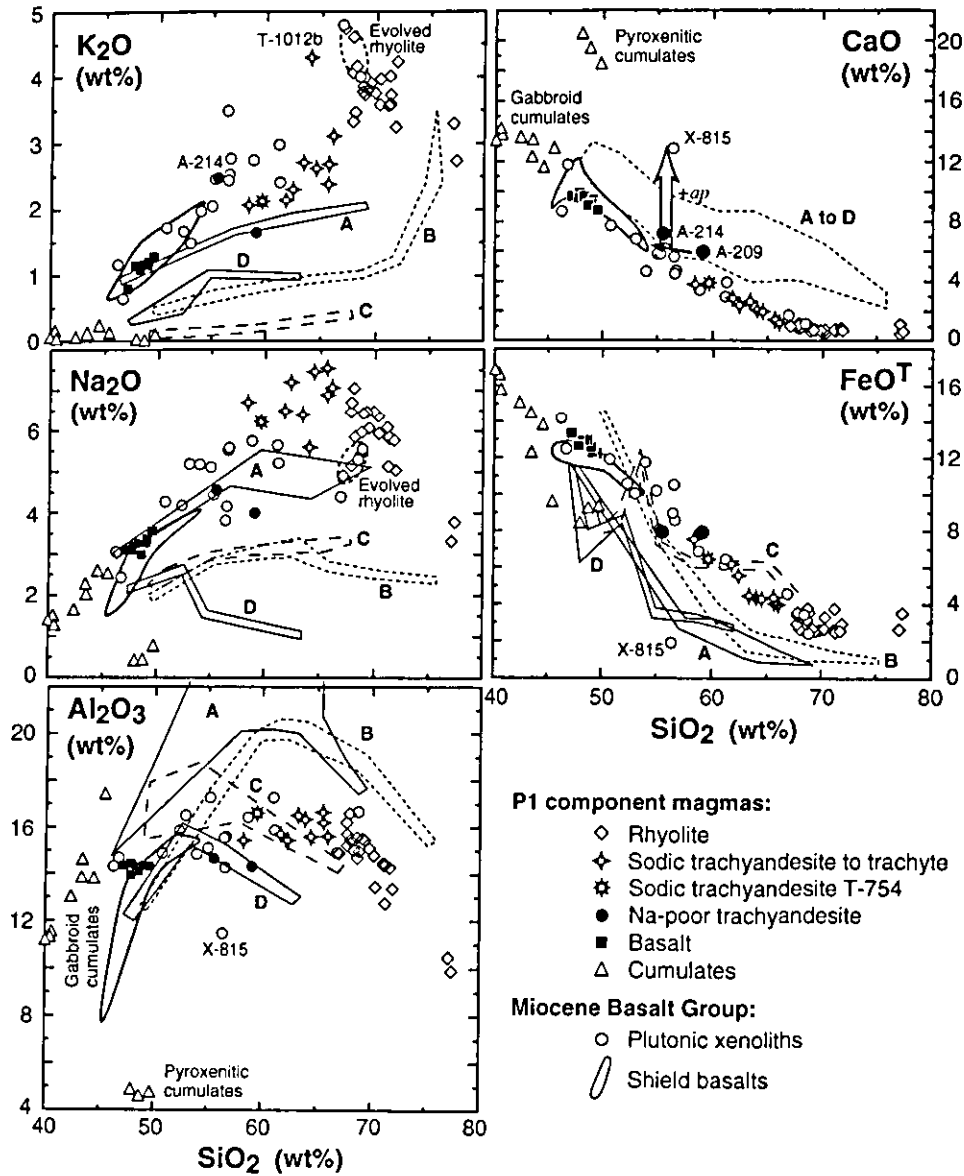
$$C_L = C_0 F^{[f(E-1)/(f-1)]} \qquad (3)$$

Figure 5. Variation of selected major elements with silica content. Note that P1 basalt differs slightly from shield basalts. Samples A-214 and A-209 of Na-poor trachyandesite, sample T-1012b of potassic trachyte, and sample X-815 of a syenite xenolith are indicated. Evolved rhyolite is marked by dashed ellipses in the K_2O and Na_2O diagrams. Elevated CaO contents of A-214 and X-815 reflect high apatite contents (open arrow +ap). Solid arrow at A-209 in CaO diagram indicates projection back onto main trend by subtraction of excess silica as discussed in the text. Outlined fields include partial melt compositions (A) from Hualalai 1801 alkali basalt, (B) from Kilauea 1921 olivine-tholeiite, both $T = 725°-1000°C$, $P_{H_2O} = 500$ MPa, $f_{O_2} = $ FMQ, hornblende-plagioclase dominated residue, both from *Helz* [1976]; (C) from Galapagos olivine-tholeiite, $T = 920°-1100°C$, $P_{fluid} = 100$ MPa, $f_{O_2} = $ G-CH, plagioclase + clinopyroxene dominated residue, from *Spulber and Rutherford* [1983]; (D) from Kilauea 1921 olivine-tholeiite, $T = 800°-1100°C$, $P_{fluid} = 500$ MPa ($H_2O:CO_2 = 3/2$ mole ratio), $f_{O_2} = $ NNO, clinopyroxene-hornblende-plagioclase dominated residue, from *Holloway and Burnham* [1972]. In the CaO diagram, all are combined in a single field for clarity. None of the experimental partial melts reproduces P1 intermediate to evolved rock compositions.

where *f* is melt fraction returned from marginal crystal mush into the main chamber, in which element concentration becomes C_L; $E = C_f/C_L$, where C_f is element concentration of residual melt in the mush; E can be approximated as $E = [D * (1 - f) + f]^{-1}$.

Table 1 compiles major elements which are not well reproduced by mass balance, and selected trace elements

which appear to be inconsistent with Rayleigh fractionation (>10% off the observed daughter concentrations) within reasonable ranges of partition coefficients (*D*), especially those so highly concentrated in daughter compositions that they exceed the maximum possible enrichment for $D = 0$. Those are generally the elements with anomalous behavior highlighted in the previous section.
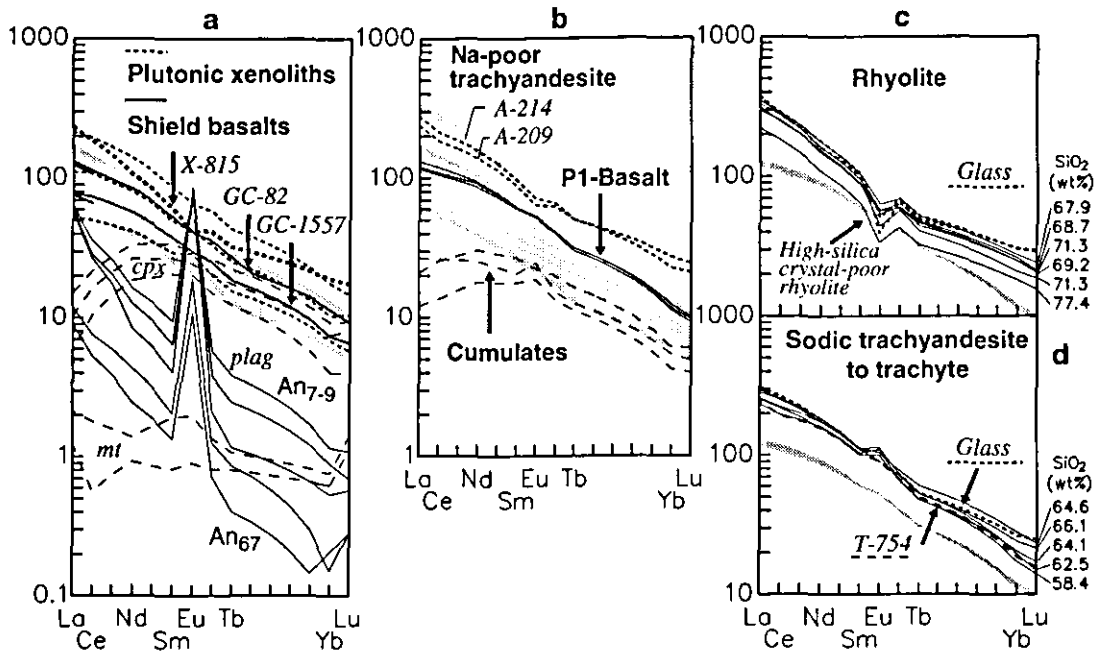
Figure 6. Rare earth element patterns. (a) Mineral separates: cumulate magnetites have near-chondritic REE concentrations; REE concentrations increase from calcic cumulate plagioclase (An_{56-67}) to oligoclase and anorthoclase (An_{7-9}) phenocrysts of trachyte and rhyolite but remain low except for light REE (LREE) and Eu. Clinopyroxene has the highest REE concentrations and controls the REE composition of LREE-depleted cumulates in Figure 6b. The gray field includes REE patterns of shield picrites to trachybasalts; picrite GC-1557 and trachybasalt GC-82 are shown for reference. Dashed lines are gabbro to monzonite xenoliths, where P-rich syenite xenolith X-815 has a pattern similar to P1 rhyolite. (b) P1 basalt is MREE-enriched with respect to the shield basalt field (gray) and has a positive Eu anomaly. Na-poor trachyandesite has high REE concentrations overlapping with P1 rhyolite (light gray field) but shows less LREE enrichment. (c) P1 rhyolite has a deep negative Eu anomaly. REE concentrations decrease from evolved through highly phyric to high-silica crystal-poor rhyolite, whereas silica content increases. Gray P1 basalt field for reference. (d) Sodic trachyandesite to trachyte with positive Eu anomaly and systematic increase in REE concentration towards higher SiO_2. The REE pattern of amphibole-bearing sodic trachyandesite T-754 is identical to the other sodic trachyandesite but has a smaller positive Eu anomaly. Light gray rhyolite and dark gray P1 basalt fields for reference. Dashed lines in Figures 6c and 6d are glass separates from rhyolite and trachyte. Only measured elements are indicated. Chondrite normalization values of La = 0.34, Ce = 0.89, Nd = 0.65, Sm = 0.209, Eu = 0.0806, Tb = 0.052, Yb = 0.225, Lu = 0.035 are averages of published ordinary chondrite data as used at K. U. Leuven (J. Hertogen, personal communication, 1989).

Crustal Partial Melts

Some of the intermediate to evolved plutonic xenoliths in P1 show evidence for partial melting, suggesting that evolved P1 rocks may have formed as crustal partial melts. At 14 Ma, the crust of the island must have consisted of an up to 7-km-thick basaltic shield volcano overlying ~7 km of Jurassic mid-ocean ridge basalt (MORB) capped by 1-2 km of Mesozoic to Miocene sediments (the thickness estimates are based on recent seismic surveys (S. Ye and R. Rihm, personal communication, 1993). The plutonic xenoliths in P1 suggest a mostly gabbroic to monzonitic intrusive complex in the interior of the island. Hence the crust provided a wide compositional spectrum of potential source rocks for partial melting. Partial crustal melts most likely would have formed under hydrous conditions. We have observed interstitial amphibole in one of the pyroxenitic cumulates, and some of the plutonic xenoliths contain amphibole or are hydrothermally altered. Partial melts from tholeiites and alkali basalts have been experimentally produced under a range of hydrous conditions (Figure 5). Compositional variations of these partial melts overlap with the P1 data for some

elements, but none reproduces P1 trends for all elements. In general, experimental partial melts are too low in K_2O, Na_2O, FeO, and TiO_2 and too high in Al_2O_3 (Figure 5). If a monzonitic source rock is assumed, hydrous partial melts would have higher K_2O content but would also be even more Al_2O_3-enriched due to the higher fraction of melting feldspar. Evolved P1 rocks do not have granite minimum melt compositions, and their trace element concentrations are not reproduced by batch melting calculations for a range of conditions (Figure 9). Furthermore, $\delta^{18}O$ values for the whole spectrum of P1 rocks lie between 5.28 to 6.81‰ (A. Freundt and J. Hoefs, unpublished data, 1992). These are identical to MORB values and show no influence from hydrothermally altered crustal rocks, as do the commonly depleted $\delta^{18}O$ values of 3.5–5.3‰ of Icelandic rhyolites [Marsh et al., 1991]. In summary, the present data do not provide evidence that the evolved P1 component magmas formed as simple partial melts of crustal rocks. We will show below, however, that such partial melts did participate in the formation of some of the P1 rocks as sources for selective contamination.
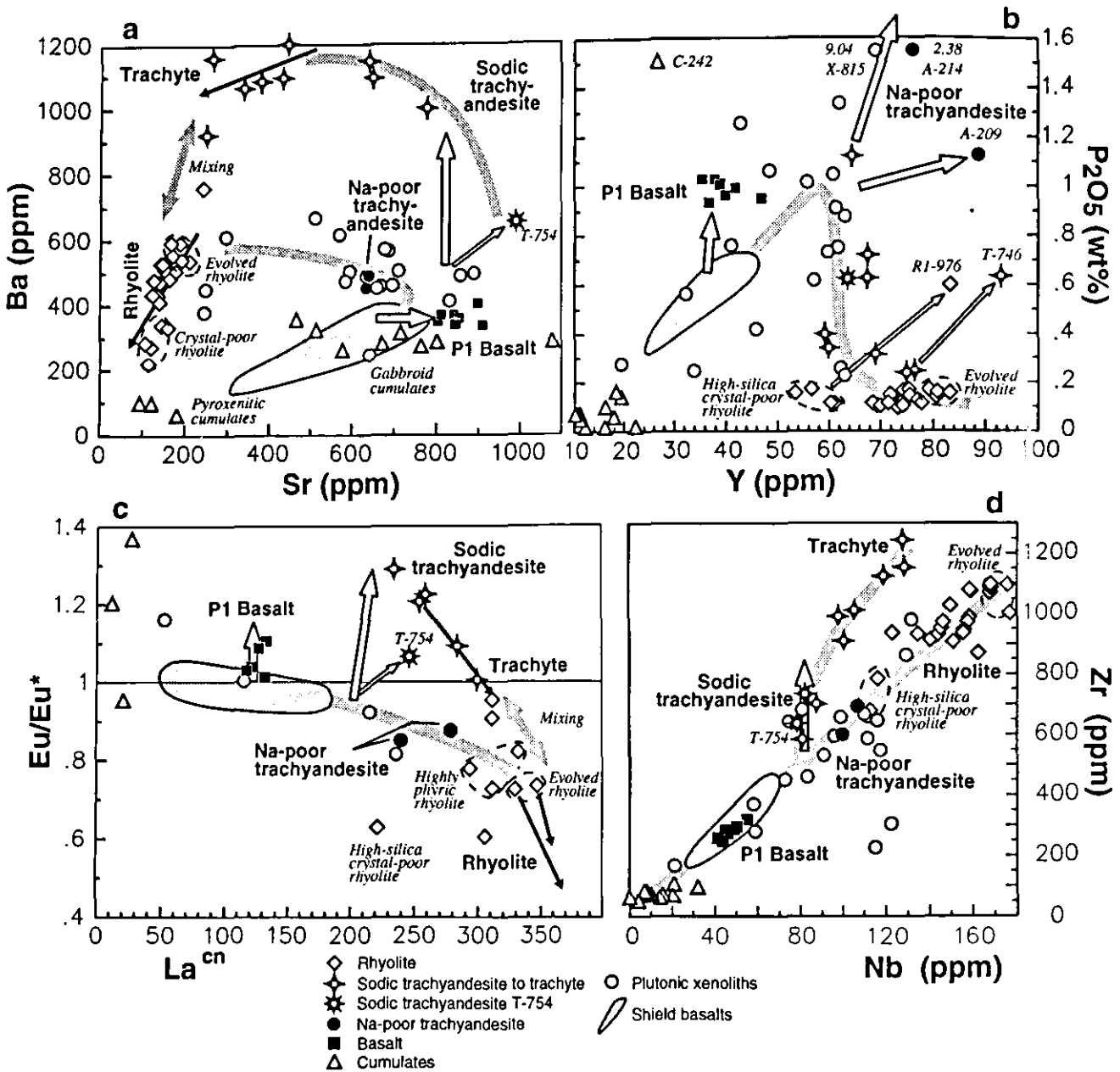
Figure 7. Minor and trace elements selectively enriched in P1 rocks. (a) Variation of large ion lithophile (LIL)-elements Ba and Sr. Both increase from mafic to evolved shield basalts (outlined field), but then Sr decreases toward more evolved compositions in response to plagioclase fractionation (lower thick gray line). Sr is distinctly high in P1 basalt and sodic trachyandesite T-754, whereas Ba is extremely concentrated in sodic trachyandesite to trachyte (open arrows). Ba and Sr are reduced by oligoclase and anorthoclase fractionation in trachyte and rhyolite (solid arrows), and these variations overlap with trachyte-rhyolite mixing effects (gray double arrow). (b) P_2O_5 variation with Y. Both show increasing concentrations in the mafic range, whereas P_2O_5 decreases above 55% silica (thick gray line is general trend). Apatite-rich cumulates such as C-242 may be responsible for P-fractionation. Open arrows point to rocks excessively enriched in P_2O_5 and partly Y, such as P1 basalt and Na-poor trachyandesite (samples A-214, A-209) but also individual, more evolved rocks. Apatite-rich xenolith X-815 could represent a possible source of contamination. High-silica crystal-poor rhyolite has lower Y concentration than the other rhyolite. (c) Size of the Eu anomaly (Eu/Eu* = $Eu_{measured}/Eu_{interpolated}$) versus chondrite-normalized La concentration. Thick gray line indicates fractionation trend toward deeper negative Eu anomaly driven by cumulates with a positive anomaly. High Eu contents in sodic trachyandesite and P1 basalt reflect contamination with feldspar (open arrows). Eu is reduced in the evolved rocks by feldspar fractionation along the solid arrows pointing from bulk rock to glass compositions. Compositional effects of rhyolite-trachyte mixing (double arrow) overlap with feldspar fractionation/accumulation effects. (d) Zr versus Nb showing all rocks along constant Zr/Nb ratio of ~6 except sodic trachyandesite to trachyte at increasing Zr/Nb (open arrow). Note reduced Zr and Nb in high-silica crystal-poor rhyolite along constant ratio and low Zr and Nb in P1 basalt compared to evolved shield basalts.

Table 1. Selected Results of Fractional Crystallization Models

	Result													
	1	2	3	4	5	6	7	8	9	10	11	12	13	14
	Shield Picrite to Trachy-basalt	Picrite to B3 Basalt	Picrite to B2 Basalt	B3 to B2 Basalt	Zonation Within B2 Basalt	P1 Basalt to Na-Poor Trachy-andesite	Shield Basalt to Na-Poor Trachy-andesite	P1 Basalt to Sodic Trachy-andesite T-754	Shield Basalt to Sodic Trachy-andesite T-754	P1 Basalt to Sodic Trachy-andesite	Sodic Trachy-andesite to Mafic Trachyte	Mafic Trachyte to Evolved Trachyte	Na-Poor Trachy-andesite to Evolved Rhyolite	Na-Poor Trachy-andesite to Evolved Rhyolite
Parent	GC-1557	GC-1557	GC-1557	B3-528	B2-1018	B2-1018	GC-82	B2-1018	GC-82	B2-1018	T-221	T-610	A-214	A-214
Daughter	GC-82	B3-528	B2-1018	B2-1018	B2-241	A-214 (−ap)	A-214 (−ap)	T-754	T-754	T-221	T-610	T-1012d	R-207	R-732
R	0.09	0.66	0.74	0.03	0.10	0.57	0.18	0.82	1.69	1.63	0.12	0.55	0.36	0.20
Percent S	53.3	45.1	47.1	5.8	10.3	48.5	42.2	47.6	41.2	51.6	23.8	22.5	35.5	46.6
Na2O								13	17	17				
K_2O		−30	−43	−10		20			−32					
P_2O_5		33	28		12	19			14	−25				
Sr		(30)	(30)					17	29					
Y	−21	−19	−13			(33)	(35)	41	35				52	54
Zr	−12	−65	−61			(30)		(26)		(12)	(17)		(13)	
Ba	−16				−12		−22			(10)	(29)			
La	−20	−15	−23			(25)	(23)	(25)	(18)				42	41
Sm	−26						(21)	35	(37)				82	84
Eu	−17	16	11				26	25	(42)	(20)			14	40
Lu	−34	−12	−22			(24)	(31)	14	(16)	19		(20)	52	56
U		−58	−34	15	12	(88)	(85)	(14)	−15	(26)	−99	(16)	−494	−629

Major element mass balance calculations: R is sum of squared residuals; percent S is solid fraction removed.

#6, 7: A-214 (−ap) means that excess apatite has been subtracted from major element composition. Positive numbers are percent element enrichment in daughter above modeled concentration. Numbers in parentheses are percent element enrichment in daughter above modeled concentration exceeding enrichment for bulk $D = 0$. Negative numbers = percent element depletion in daughter below modeled concentration.
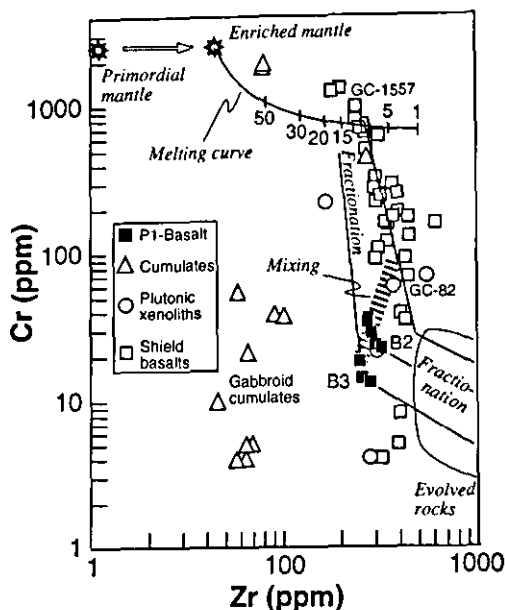
Figure 8. Cr-Zr diagram showing fractional crystallization (solid lines) from primitive to evolved basalt, controlled by pyroxenitic cumulates, and on to more evolved rocks (gray field), controlled by gabbroid cumulates. P1 basalt B3 is probably derived from a more depleted source (i.e., melting curve shifted to the left) rather than from a higher degree of melting. B2 basalt can be explained by mixing of B3 magma with fractionated shield basalt melt (dashed bar). The melting curve (numbers give percent melting) for an enriched mantle source relative to Zr-poor primordial mantle [*Wood*, 1979] is adjusted to fit 10% partial melting for shield picrites, which has been determined from molar MgO and FeO concentrations after *Hanson and Langmuir* [1978]. For comparison, Ce/Yb$_{cn}$ = 8 to 11 of the basalts requires 8–10% batch melting of a 25% garnet-bearing mantle peridotite source at >2 GPa [*Wyllie*, 1979]. K, Rb, and P concentrations could be generated by 8%, 5%, and 12% batch melting (D = 0) without residual phlogopite.

Shield Basalts

Primitive parental melts of the shield basalts originated in a garnet-bearing mantle source as indicated by Ce/Yb$_{cn}$ ratios between 8 and 11 (Figure 6a). *Hoernle and Schmincke* [1993a] have shown that more evolved basalt magmas can be derived from picritic melts by olivine-clinopyroxene removal (at MgO > 6 wt %) and by clinopyroxene-plagioclase-oxide-apatite fractionation (at MgO < 6 wt %). A calculated fractionated assemblage (53%; result 1 in Table 1) closely resembles pyroxenitic cumulates found in P1. Th/Ta ratios of 0.93 to 1.45 do not allow for significant contamination of the basalts with high Th/Ta marine sediments. We have found no indications for contamination by Jurassic MOR basalts, such as higher Zr/Nb ratios. These conclusions are supported by isotope data [*Hoernle et al.*, 1991; *Cousens et al.*, 1990]. The magma plumbing system thus seems to have been insulated against marine sediments and older crust; it may have been confined to the intrusive core of the shield.

P1 Basalt

P1 basalt comprises two compositionally distinct magma batches, B2 basalt and B3 basalt. B2 basalt is slightly more evolved than B3 basalt, but it cannot be derived from B3

basalt by crystal fractionation (result 4 in Table 1), because it has higher concentrations of compatible trace elements, such as Cr, at similar or higher concentrations of incompatible trace elements, such as Zr (Figure 8). B3 basalt also has slightly higher REE concentrations (e.g., La = 41.1 ppm, Yb = 2.59 ppm) than B2 basalt (La = 39.8 ppm, Yb = 2.51 ppm). The compositional zonation within B2 basalt is, on the other hand, consistent with crystal fractionation (result 5 in Table 1). Though the major element compositions of both types of P1 basalt can be derived from primitive shield basalt by crystal fractionation similar to evolved shield basalts, trace element modelling requires a parental composition less rich in incompatible trace elements than shield picrite GC-1557 (results 2 and 3 in Table 1). The need for a "depleted" parental composition is clearly illustrated in the Cr-Zr diagram (Figure 8). Generation of this parental melt would require a higher degree of mantle melting or a more depleted mantle source composition. Considering the amount of melt generation involved in the construction of the >2 × 10^4 km^3 basaltic shield, a depletion of the mantle source with time seems the more plausible explanation. The differences between B3 and B2 basalts could be attributed to minor differences in mantle melting conditions, but since these magmas are so closely related in space and time to each other as well as to the shield basalt magmas, we prefer to interpret B2 basalt as a mixture between B3 basalt magma and a shield basalt melt (Figure 8). Since there was no substantial hiatus between P1 and the terminal shield lavas, shield basalt magma could well have been available at depth, and we will show below that the presence of both types of basalt magmas is required to explain the generation of the more evolved rocks.

High Sr and slightly elevated Ba (Figure 7a), a positive Eu anomaly (Figure 7c), and a higher Na$_2$O content relative to shield basalts (Figure 5) suggest that P1 basalt is contaminated with an intermediate to sodic plagioclase component. About 10 wt % of an assimilated plagioclase component (An$_{30-60}$, 2000 ppm Sr, 12 ppm Eu) would generate the ~150 ppm excess Sr of P1 basalt relative to shield mugearite and would be consistent with observed Al$_2$O$_3$, CaO, Na$_2$O, K$_2$O, and Eu contents. This contamination is distinct from the syneruptive admixing of rhyolite to the P1 basalt [*Freundt and Schmincke*, 1992], because (1) here we refer to basalt samples not containing any visible rhyolite, and (2) dissolved rhyolite would not increase the Na/K ratio and it would reduce, rather than increase, Sr and Eu concentrations. The excess P$_2$O$_5$ content of P1 basalt (Figure 7b) suggests contamination from a P-rich crustal source. Assimilation of 0.8 wt % apatite corresponding to 0.35 wt % excess P$_2$O$_5$ would explain the increased MREE concentrations in P1 basalt (Figure 6b).

P1 Na-Poor Trachyandesite

This component magma is represented by two samples (A-209, A-214), which have virtually identical modal and mineral compositions. The higher SiO$_2$ content of A-209 (59.1 wt %) is merely an artifact of our inability to completely remove silica-filled vesicles during sample preparation. If we shift back A-209 to ~53 wt % SiO$_2$, all other elements are projected back onto the general trends in variation diagrams (Figure 5) and A-209 would be slightly more mafic than A-214 (55.5 wt % SiO$_2$). Both samples clearly contain excess P$_2$O$_5$ (Figure 7b) and A-214 has an
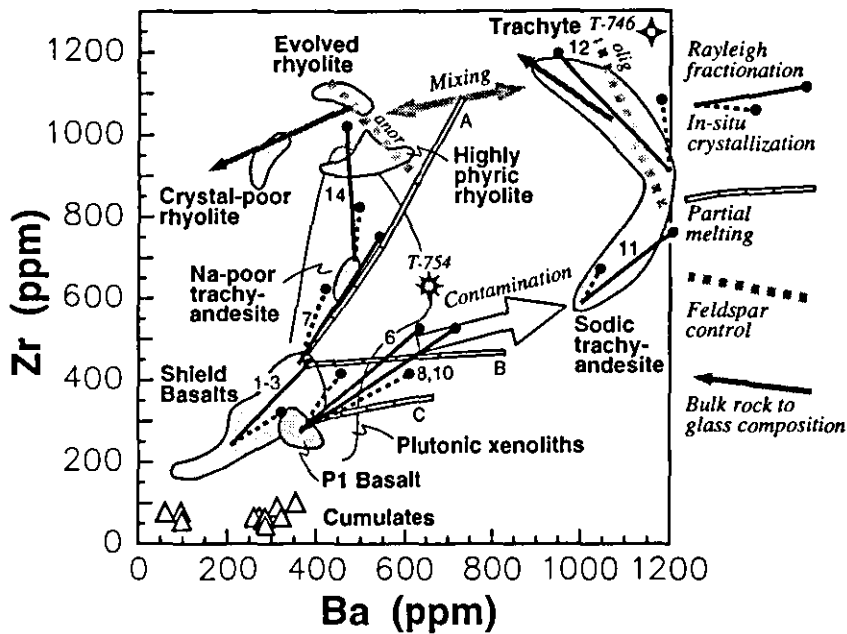
Figure 9. Zr-Ba diagram illustrating the results of fractionation and melting model calculations, which are qualitatively similar for other HFS and large ion lithophile (LIL) elements. Also shown are major contamination of sodic trachyandesite (open arrow), the compositional controls of anorthoclase (anor) and oligoclase (olig) fractionation or accumulation in rhyolite and trachyte (bold gray dashed lines), the fractionation from bulk rock to matrix glass of rhyolite and trachyte (thin gray arrows), and mixing between rhyolite and trachyte (gray double arrow). Numbers at the Rayleigh fractionation (after equation (2); solid line with dot) and in situ crystallization paths (after equation (3) with $f = 0.05$; dashed line with dot) refer to the calculations in Table 1. None of the fractionation calculations reproduces sodic trachyandesite. Rayleigh fractionation is generally more successful in reproducing observed daughter compositions than in situ crystallization, which does not sufficiently enrich incompatible trace elements. This could be countered by increasing the value of f, but then the two models become chemically indistinguishable. White lines for batch partial melting (after equation (1)) of (A) anhydrous trachybasalt, (B) hydrous trachybasalt, and (C) hydrous monzonite have tick marks at 10% melting intervals. Partition coefficients and melting mineral assemblages are available as electronic supplement. All calculated paths extend to the F values obtained by mass balance calculations (Table 1). Melting curves do not yield P1 evolved rock compositions.

elevated CaO content (Figure 5), reflecting contamination with 3 (A-214) and 0.5 wt % (A-209) of an apatite component. Apatite contamination increased middle and heavy REE concentrations in these rocks to almost P1 rhyolite level (Figure 6b). U is excessively enriched to 5.6 (A-209) and 14.2 ppm (A-214), whereas all other rocks have U < 4.3 ppm. Though A-209 is less P enriched, it is richer in Y (Figure 7b) and the MREE than A-214. Hence the apatite components affecting these rocks had different trace element compositions.

Direct derivation of A-214 from basaltic compositions by mass balance calculations gave poor results especially for P_2O_5; we thus assumed that apatite contamination happened after fractionation and subtracted 3 wt % apatite from the major elements. The resulting derivation of A-214 from either shield or P1 basalt (results 6 and 7 in Table 1) yields similar cumulate compositions comparable to observed gabbroic cumulates. Since the trace element compositions of the apatite contaminants are unknown, we could not correct the trace elements for the effect of added apatite. Therefore excess REE and Y contents relative to Rayleigh fractionation results (results 6 and 7 in Table 1) are to be expected. HFS elements, which are not incorporated in apatite, exceed calculated enrichments from P1 basalt (result 6 in Table 1)

and suggest high field strength element (HFSE) enriched shield basalt as the more likely parent (compare fractionation paths 6 and 7 in Figure 9).

P1 Sodic Trachyandesite to Trachyte

Nb, Y, Ta, Th, U, Rb, and K_2O concentrations in sodic trachyandesite (including T-754) are fairly low compared to other rocks of similar silica content, suggesting a parental mafic magma relatively depleted in these elements. Correspondingly, fractionation models reproduce observed concentrations of sodic trachyandesite better for a P1 basalt than for a shield basalt parental composition (Figure 9 and results 8–10 in Table 1). The apparent REE and Y enrichment over calculated concentrations (result 8 in Table 1) is an artifact of the apatite contamination of P1 basalt; the true parent magma would have had lower contents of P_2O_5, REE, Y, and U. Fractionation from P1 basalt is further supported by almost parallel REE patterns of sodic trachyandesite and P1 basalt (Figure 6d) and by changes in REE ratios that are consistent with fractionation of the gabbroic cumulates. The fractionation process is better described by the Rayleigh formulation, because ratios of elements with different D values (such as Eu/Th, La/Th, La/Ba, Zr/Ba) tend to diverge away from sodic trachyandesite values for in
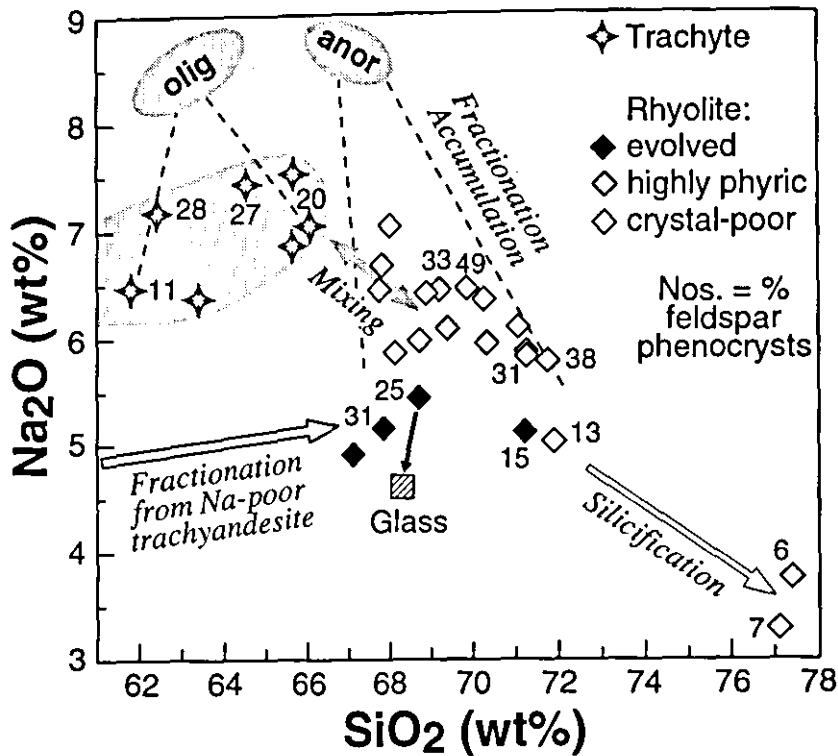
Figure 10. The Na_2O-SiO_2 diagram illustrates the compositional control of variable oligoclase and anorthoclase fractionation or accumulation on trachyte and rhyolite by dashed lines radiating from feldspar compositional fields. Light shading is entire range of feldspar microprobe data; dark ellipse is dominant composition of oligoclase (olig) and anorthoclase (anor). Anorthoclase accumulation in a range of evolved rhyolite compositions forms highly phyric rhyolite. Anorthoclase fractionation similarly produces crystal-poor rhyolite analogous to the bulk rock to glass trend (thin solid arrow), but most of the crystal-poor rhyolite samples seem to be affected by mixing with trachyte (gray double arrow). Sodium is diluted by silicification in high-silica crystal-poor rhyolite.

situ crystallization (Figure 9). Oligoclase-dominated fractionation from sodic trachyandesite through mafic to evolved trachyte is supported by (1) model calculations (results 11 and 12 in Table 1), (2) parallel REE patterns and REE concentrations increasing systematically with silica content (Figure 6d), (3) by changes in REE ratios in agreement with such fractionation, and (4) by identical oligoclase phenocryst compositions across the whole compositional interval (Figure 3). Rayleigh models describe this fractionation better than in situ crystallization models (Figure 9).

Sodic trachyandesite has excess concentrations of Na_2O, Zr, Ba, and Eu and Sr in T-754, which are inconsistent with crystal fractionation from basalt (Figures 5 and 7 and results 8–10 in Table 1). Excess P_2O_5, Y, M + HREE, and U occur in one trachyte sample (T-746, Figure 7b), and excess K_2O in another (T-1012b, Figure 5). Selective enrichment of these elements suggests contamination with feldspar, zircon and apatite components. REE concentrations in sodic trachyandesite as high as those in the rhyolite and with a slightly concave-up pattern (Figure 6d) may be partly due to L + MREE contribution from the feldspar contaminant and M + HREE contribution from the zircon contaminant [cf. *Hinton and Upton*, 1991]. We were unable to identify appropriate feldspar xenocrysts in these rocks. Zircon crystals are also not observed, but apatite is present. Contamination has most strongly affected the sodic trachyandesite, and the concentrations of Na_2O, Ba, and Eu decrease toward evolved

trachyte in response to oligoclase fractionation. However, some trachyte samples have Zr and Ba contents above those predicted by fractionation calculations. Also, identical oligoclase compositions of K-rich (T-1012b) and sodic trachyte indicate K enrichment after feldspar crystallization. Thus some contamination continued during sodic trachyandesite to trachyte fractionation but affected only partial batches of the evolved trachyte with K, Zr, or Ba.

The chemical effects of mixing between P1 trachyte and rhyolite during crystallization (Figure 3) are difficult to quantify because they overlap with effects such as Na_2O, Eu and Ba depletion by oligoclase fractionation (Figures 10, 7a and 7c). Assimilation of rhyolite anorthoclase during mixing cannot be responsible for the Eu enrichment of sodic trachyandesite, because its Eu concentration is too low (Figure 6a). The MREE-enriched REE patterns of trachyte do not seem to be influenced by the MREE-depleted rhyolite composition (Figure 6d), suggesting that only small rhyolite fractions were admixed.

P1 Rhyolite

P1 rhyolite cannot be derived by crystal fractionation from sodic trachyandesite to trachyte, because Na_2O, Ba, Sr, Eu, Zr, and most REE would have to be depleted by feldspar-dominated fractionation, while at the same time elements such as K_2O, Nb, and Th should be enriched. The rhyolite data also do not follow the calculated paths of hydrous batch

melting involving residual amphibole (Figure 9). Ratios of HFS trace elements (which are not affected by apatite assimilation) of rhyolite and Na-poor trachyandesite are very similar (e.g., Figure 7d), and both rock types seem to follow the same trends in variation diagrams (Figures 5, 7a, 7c, and 7d). Mass balance calculations (results 13 and 14 in Table 1) confirm fractionation of rhyolite from Na-poor trachyandesite. Rhyolite Y and REE contents are not reproduced when the fractionation calculation has to account for the excess P_2O_5 content of Na-poor trachyandesite by including 12–16% apatite into the cumulate (results 13 and 14 in Table 1). Also, the concave-up rhyolite REE pattern contrasts with the apatite-induced MREE-enriched Na-poor trachyandesite pattern (Figures 6b and 6c). Rayleigh fractionation paths based on apatite-poor cumulate reproduce rhyolite trace element compositions well, whereas the in situ approach does not sufficiently enrich HFS elements (Figure 9).

Highly phyric rhyolite is formed by up to 20 wt % anorthoclase accumulation to a range of evolved rhyolite compositions (Figure 10), diluting incompatible elements such as Zr and REE (Figures 6c and 7d) and slightly increasing Eu (Figure 7c). Many of the rhyolite samples that plot into the wedge between evolved rhyolite, highly phyric rhyolite, and the trachyte field in Figure 10 contain trachyte-derived augite crystals [*Freundt and Schmincke*, 1992] and show subtle increases especially in Eu and Ba concentration (Figures 7a and 7c). These samples are variably affected by mixing between a range of rhyolite compositions and trachyte. Anorthoclase-dominated fractionation generates crystal-poor rhyolite along trends parallel to the matrix-glass arrow in Figure 10. The very high silica content of crystal-poor rhyolite from the base of P1 reflects silicification during devitrification of the vitric shards, diluting other elements along constant ratios (Figures 6c, 7c, and 7d) but leaving phenocrysts unaffected. If any mobilization of (alkali) elements occurred during this process, it is obscured by the effects of anorthoclase fractionation. One sample of high-silica crystal-poor rhyolite (R1-976) is contaminated by a Y-rich apatite component (Figure 7b).

Processes of Selective Contamination

Most P1 component magmas have been variably affected by selective element contamination from three types of sources: a feldspar source contributing Na, (K), Ba, (Sr), and Eu, a zircon source contributing Zr, Hf, (REE), and an apatite source contributing P, Y, (M)REE, and U.

Feldspar Source

P1 basaltic melt in contact with melted granite could be enriched in Na_2O [*Johnston and Wyllie*, 1988], provided that the activity of Na_2O in the basaltic melt is lower than in the partial melt [*Watson and Jurewicz*, 1984]. Sodic to intermediate plagioclase in contact with the basaltic magma, which is in equilibrium with more calcic plagioclase, would partially dissolve and preferentially enrich the magma in albite component [*Donaldson*, 1985; *Tsuchiyama*, 1985]. Diffusion of Sr (and possibly Eu and Ba) in albitic feldspar ($10^{-1.6}$ cm^2/s [*Giletti*, 1991]) is significantly faster than Na and K diffusion ($\sim 10^{-9}$ to 10^{-12} cm^2/s [*Grove et al.*, 1984]) and thus facilitates preferential enrichment in the melt. Applying these considerations to P1 sodic trachyandesite, the contam-

inating feldspar component must have been more albitic than the oligoclase phenocrysts (Figure 3). The strong zonation of the oligoclase phenocrysts could thus be due to the combined effects of fractionation and Na_2O enrichment. However, neither stoichiometric albite nor granite minimum melt (<6 wt % Na_2O) satisfy mass balance calculations or define reasonable mixing lines with sodic trachyandesite. Even though Sr, Eu, and Ba may rapidly migrate out of dissolving feldspar, their diffusion in melt (10^{-10} to 10^{-11} cm^2/s) is much slower than that of Na (10^{-7} cm^2/s [*Hofmann*, 1980]) and would require extended contact with the source, though diffusion might be faster in hydrous melt [cf. *Watson*, 1981]. Therefore we propose (1) that mixing with a low-degree partial melt already strongly preenriched in Na, Ba, and Eu by partial dissolution of, and rapid diffusion from, sodic feldspar occurred, and (2) that selective contamination of sodic trachyandesite magma must have operated under conditions that maximized the contact area for exchange by diffusive and mechanical mixing and minimized the magma depth to be affected. Such conditions could be flow through a conduit or fissure, or sodic trachyandesite magma draping the chamber walls.

Zircon Source

Zr is excessively enriched over other HFS elements in sodic trachyandesite and trachyte; Zr/Hf = 47–56 is higher than in the other rocks where Zr/Hf < 46. This indicates dissolution of zircon, which has high Zr/HFSE ratios (e.g., Zr/Hf = 25–100 [*Mahood and Hildreth*, 1983]). Hydrous melting can rapidly dissolve zircon (100 μm grain in 500 years under 750°C and 6 wt % H_2O [*Harrison and Watson*, 1983]), but source rocks with >100 ppm Zr will always retain residual zircon since Zr solubility in partial melt is <500 ppm Zr at T < 900°C [*Watson and Harrison*, 1983]. Simple admixing of crustal partial melts thus cannot be responsible for Zr enrichment of sodic trachyandesite to trachyte magma to concentrations of 600–1250 ppm. Despite such high concentrations, this magma remained undersaturated in Zr because zircon crystals were not precipitated. Zr would therefore have diffused into the undersaturated sodic trachyandesite magma but even the fastest diffusivity of $\sim 10^{-9}$ cm^2/s in hydrous melt [*Harrison and Watson*, 1983] is only of the order of silica diffusion and would thus not allow for selective enrichment. Addition of only 0.5 wt % zircon would accommodate the 250-ppm Zr increase away from the general Zr/Nb trend to sodic trachyandesite in Figure 7d. We therefore envisage that albitic partial melt carried zircon crystals into the sodic trachyandesite-trachyte magma, where they rapidly dissolved. Many of the plutonic xenoliths contain traces of zircon, and zircon-rich restites may have formed during previous melting events.

Apatite Source

Apatite contamination affected the entire P1 basalt but only small local batches of the more evolved magmas. The contaminating apatite sources had different trace element compositions. P1 basalt magma has been contaminated with the least Y-REE rich apatite, which seems to correlate with its ability to melt less evolved crustal rocks. Apatite crystals (100 μm) could dissolve 5 times faster (20 years) than zircon crystals under the same hydrous melting conditions (6 wt % H_2O at 750°C [*Harrison and Watson*, 1984]), but again the melt needs to be apatite-undersaturated in order to become

P-enriched by diffusion, and this is commonly not the case in felsic crustal partial melts [*Watson and Capobianco*, 1981]. Basalt remains well below its 2 wt % P_2O_5 (for $T = 1100°C$ [*Harrison and Watson*, 1984]) solubility limit (Figure 7b) but does contain apatite which is, however, mostly included in other phenocrysts and may have precipitated in response to local saturation [*Bacon*, 1989]. Phosphorous could thus diffuse into the basaltic melt from any saturated source but the process would be limited by very slow P diffusivity ($\sim 10^{-10}$ cm^2/s [*Harrison and Watson*, 1984]), unless apatite crystals were intensely mechanically mixed into the melt before dissolution. The intermediate to evolved rocks all contain apatite, suggesting P_2O_5 saturation, and they exceed the solubility limit of 0.1–0.5 wt % P_2O_5 (at $T = 900°C$) after *Harrison and Watson* [1984]. Phosphorous thus could not have diffused into these melts but must have been introduced by incorporation of apatite crystals. The occurrence of a partially molten syenite xenolith (X-815: 9.04 wt % P_2O_5, 26 ppm U; Figure 7b) consisting almost entirely of potassic oligoclase and apatite (21%) shows that potential apatite-rich source rocks were available along the magma ascent path. Local apatite residues from previous crustal melting events [cf. *Watson and Capobianco*, 1981] may have contaminated batches of viscous magma.

Selective element contamination has also been reported from other volcanoes, where it is attributed either to rapid diffusion along a gradient in chemical potential [*Macdonald et al.*, 1987; *Blichert-Toft et al.*, 1992] or to influx of a fluid phase [*Clocchiatti et al.*, 1988]. In the case of P1, little variation of highly soluble elements such as U and of oxygen isotopes (as mentioned above) give no indication to involvement of hydrothermal fluids. Also, selective contaminations did not only involve highly mobile alkali elements but also elements with very low diffusivities. Furthermore, saturation conditions varied for different elements and magma compositions. Selective contamination thus cannot have been exclusively diffusion-controlled. It is rather necessary to invoke more complex processes involving selective diffusion of Na, Ba, and Eu from feldspar crystals into partial melt, possibly selective diffusion from partially molten crust or xenoliths into the magma, mixing of magma with such partial melts carrying zircon and/or apatite crystals, and eventually dissolution of these crystals in the magma provided it is undersaturated in the particular component.

Formation of Compositional Gaps

Compositional gaps in magmatic series, originally recognized by *Bunsen* [1851] and *Daly* [1925], are a prominent feature of the volcanic rocks on Gran Canaria [*Schmincke*, 1967, 1969a, b]. Miocene rocks overlying P1 are all highly evolved with few intercalated basalts but no intermediate rocks. P1 does contain a subordinate fraction of intermediate trachyandesitic rocks but compositional gaps exist between basalt and Na-poor trachyandesite or sodic trachyandesite (spanning 6 and 9 wt % SiO_2, respectively) and between Na-poor trachyandesite and rhyolite (9 wt % SiO_2), whereas the sodic trachyandesite to trachyte series is continuous (Figure 5). Partial melting of sialic crust intruded by basaltic melts has been invoked as a process to form compositional gaps in volcanic sequences [e.g., *Patchett*, 1980; *Myers and Marsh*, 1981; *Mahood and Halliday*, 1988; *Huppert and Sparks*, 1988a, b]. Crustal partial melting generated selective

contamination of P1 magmas and thus widened compositional gaps for selected elements, notably at the transition from basalt to sodic trachyandesite. Inhibited extraction of intermediate magmas due to their rheological properties [e.g., *Cann*, 1968; *Jones*, 1979; *Schmincke*, 1990] also played a role in the P1 case, because the density of the intermediate P1 magmas is high, and the density of Na-poor trachyandesite magma in particular exceeds that of the basalt magma [*Freundt and Schmincke*, 1992, Figure 11]. Also, intermediate magmas formed in the plutonic environment but were unable to erupt. The P1 magma plumbing system involved two reservoirs, a shallow silicic and a deep-seated basaltic chamber. This facilitated replenishment of the silicic chamber with basaltic melt, which was stored under high temperature in the deeper reservoir, and thus created the "bimodality" of the P1 ignimbrite. We have shown that fractional crystallization was the major process of differentiation of the P1 magmas, and special conditions of fractional crystallization can potentially cause compositional gaps. Sections with a flat gradient in the liquidus temperature variation over composition imply a strong compositional change across a small temperature interval [*Nockolds*, 1936; *Willie*, 1963; *Grove and Donnelly-Nolan*, 1986]. The volume fraction of magmas compositionally corresponding to such sections would be small. Experimental determination of the liquidus curves of P1 magmas would be needed to verify flat gradients across the compositional intervals marked by gaps. Fluid-dynamical processes of fractional crystallization may also be invoked, such as compositional convection of boundary layers forming chemically distinct top zones in magma chambers [e.g., *Chen and Turner*, 1980; *McBirney et al.*, 1985], or sudden massive sedimentation of crystals which previously remained suspended over the intermediate interval [*Brophy*, 1991; cf. *Koyaguchi et al.*, 1993]. The formation of compositional gaps in P1 thus cannot be attributed to a single process, and our continuing work aims at an evaluation of the importance of the various processes involved.

Magmatic Evolution and Chamber Emplacement

The formation of highly differentiated magmas by fractional crystallization or crustal melting is a fundamental problem of ocean island petrology. On Iceland, for example, rhyolites are believed to represent crustal melts [e.g., *Marsh et al.*, 1991], but Iceland is in a unique tectonic setting where a hotspot coincides with the Mid-Atlantic Ridge and crustal subsidence rates are very high. The almost complete absence of rhyolite on the Hawaiian Islands is attributed to high supply rates of mafic magma (>0.01 km^3/yr) from the mantle, holding crustal reservoir temperatures well above the basaltic solidus [*Shaw*, 1985]. The long-term evolution ($\sim$15–13.5 Ma) of mafic magma compositions from picrite through tholeiite and alkali basalt to nephelinite during the Miocene magmatic cycle of Gran Canaria reflects decreasing degrees of mantle melting [*Hoernle and Schmincke*, 1993b]. Magma supply rates decreased from >0.01 to <0.002 km^3/yr at the end of the Miocene basaltic shield phase [*Bogaard et al.*, 1988], and the island became capped by >800 km^3 of evolved volcanic rocks. The sudden transition from basaltic to silicic volcanism at 14 Ma, marked by the emplacement of composite flow P1, does not reflect a similarly instantaneous change in magmatic evolution because intermediate to evolved intrusive magmas had formed earlier but were unable to erupt.

Crystal fractionation controlled the differentiation of the shield basalt magmas and the evolved Miocene magmas [*Hoernle and Schmincke*, 1993a; *Schmincke*, 1969b, 1990; *Cousens et al.*, 1990] as well as of the P1 component magmas. However, partial melting of crustal wall rocks, which was probably related to emplacement of the P1 magma chamber, provided selective contamination of most of the P1 component magmas. Such contamination combined with the coexistence of different parental basaltic melts generated two contemporaneous differentiation series (Figure 11):

Series I is derived from shield-like basalt magma, which differentiated to Na-poor trachyandesite which, in turn, was parental to rhyolite. The Na-poor trachyandesite became at least partially contaminated with apatite.

Series II involved a P1 basalt-like parental magma that was depleted in incompatible trace elements and differentiated to trachyandesite. Composition of this trachyandesite was strongly modified by selective enrichment with mainly Na to form sodic trachyandesite and generate a sodic fractionation series through mafic to evolved trachyte.

Both types of mafic parental magmas (shield basalt, B3-type P1 basalt) appear to have been available contemporaneously; B2-type P1 basalt can well be explained by mixing between these magmas in a deep-seated reservoir. The more evolved magmas, however, differentiated at a shallow crustal level. The depth at which magma density equals country rock density is most suitable for emplacement of a crustal magma chamber [*Ryan*, 1987]. The density of basaltic volcanic rocks increases with the depth of burial, whereas the density of the plutonic core of largely intermediate, feldspar-rich composition is probably more uniform with depth. Conversion of crustal seismic velocities [from *Banda et al.*, 1981, Figure 14] to rock densities after *Christensen and Shaw* [1970] yields a <2-km-thin top layer ($\rho = 2395$ kg/m^3) overlying seismically uniform crust ($\rho = 2857$–2890 kg/m^3) extending down to the Moho. Evolved basaltic melts with densities of 2600–2650 kg/m^3 [cf. *Freundt and Schmincke*, 1992] would thus have ponded very high in the crust to form the P1 magma chamber. Storage of mafic magma at the base of the crust must have been controlled by other factors than density relations, probably by thermal conditions and the stress regime at the mantle/crust boundary [cf. *Gudmundsson*, 1990].

A Summary Scenario

We have previously discussed the zonation pattern of the P1 magma chamber at the time of eruption, based on mixing patterns, withdrawal systematics and density relations, arriving at a chamber model in which a marginal sheath of vertically zoned trachyte to sodic trachyandesite along the chamber walls mantles a central core of rhyolite magma [*Freundt and Schmincke*, 1992]. The present study supports this model for the following reasons: (1) Sodic trachyandesite to trachyte has been most strongly and persistently affected by contamination, and the contamination processes require extended contact with the wallrocks over a large area. Rhyolite remained unaffected by contamination, except for very local apatite incorporation into crystal-poor rhyolite at the chamber top. (2) No substantial temperature gradient within the rhyolite volume is evident from mineral thermometry, but trachytic magma appears to have been
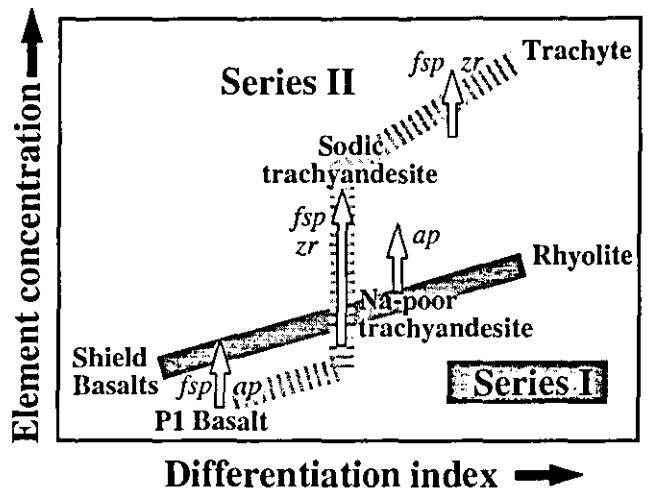

Figure 11. Schematic illustration of the chemical evolution of the two fractionation series and the influence of contaminating feldspar (fsp), zircon (zr), and apatite (ap) components (open arrows) as discussed in the text. Notable features include the incompatible element-poor composition of P1 basalt compared to shield basalts and the contamination-induced jump to sodic trachyandesitic composition in the intermediate range.

slightly cooler and more oxidized than rhyolitic magma (Figure 4). In our model of concentric zonation, the thermal boundary layer of the magma chamber would lie within the trachytic rim zone and the central rhyolite volume would be insulated against wallrock contamination.

Combining the results of the present study with those of *Freundt and Schmincke* [1992], we can summarize, in a rather simplified scenario, the sequence of events that led to the formation of the two magma series and the zonation pattern of the magma assemblage in the P1 reservoir (Figure 12). The timing of events cannot be entirely resolved by the data at hand, and there may have existed several conduits connecting the upper crustal chamber with one or more deep-seated reservoirs. Stage I encompasses emplacement of a shallow crustal reservoir and differentiation of shield basalt magma to Na-poor trachyandesitic magma parental to P1 rhyolite. Since we could only recover two samples of Na-poor trachyandesite, we have little information about possible contamination of this magma batch during this stage. The reservoir at the base of the crust is replenished with melt derived from a depleted mantle source (B3 basalt), which mixes with resident mafic melt to form B2 basalt. Basaltic melt is strongly contaminated by heated wallrocks. In stage II, another trachyandesite magma derived from depleted basaltic melt changes in composition to sodic trachyandesite due to strong contamination either on its way to the upper chamber or within it. Owing to its intermediate density, this magma is then sandwiched between Na-poor trachyandesite and rhyolite magma in the P1 reservoir. While sodic trachyandesite differentiates to trachyte, rhyolite magma continues to crystallize and becomes zoned into a thin crystal-poor top zone and a main volume of crystal-rich magma containing accumulated anorthoclase. During stage III, high crystallinity raises the rhyolite magma density above that of the trachyte magma and the sinking highly viscous rhyolite plug squeezes trachyte magma up along the
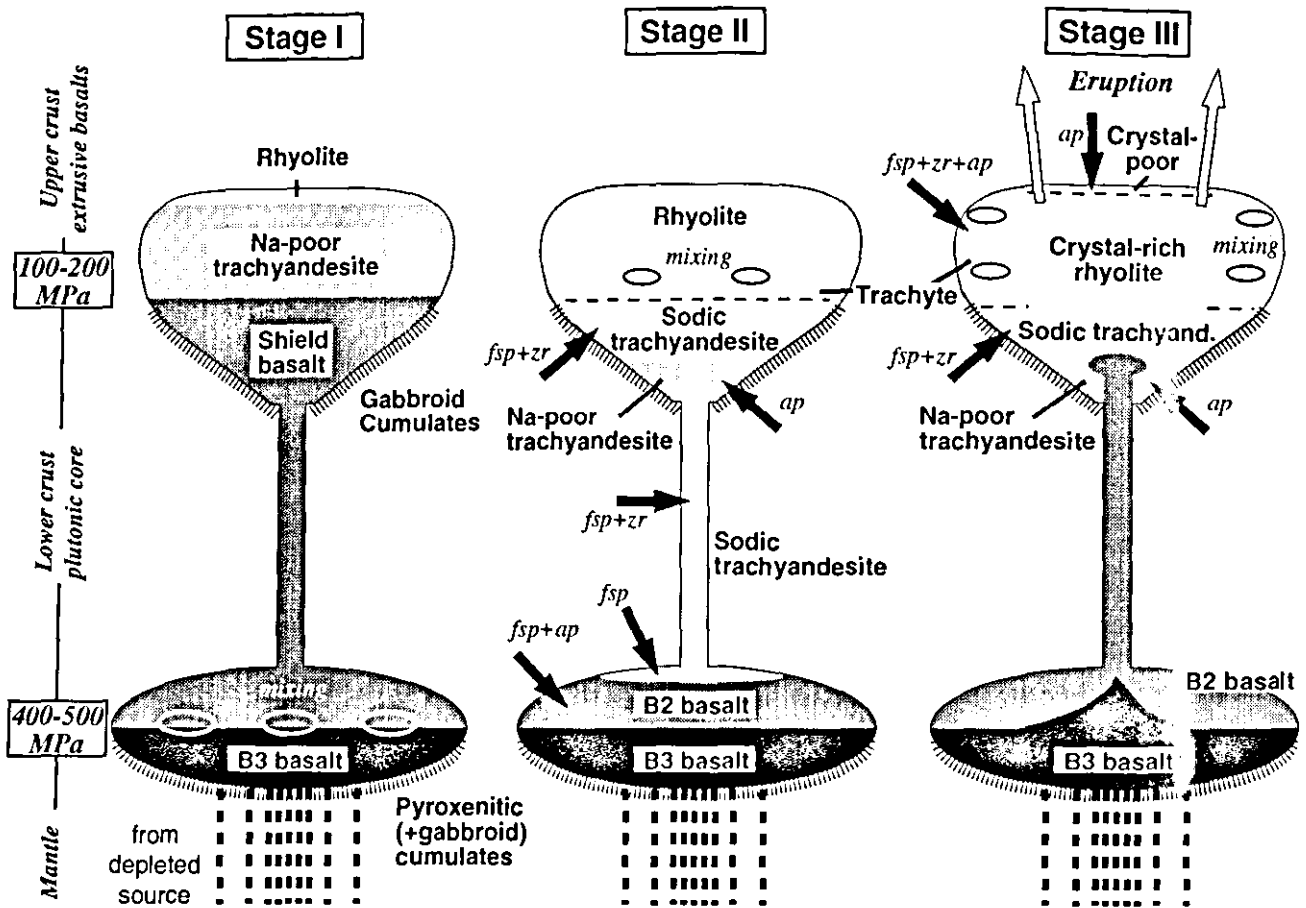
Figure 12. Illustration of the evolution of P1 component magmas in a lower and an upper crustal reservoir as discussed in the text. Solid arrows indicate contamination with feldspar (fsp), zircon (zr), and apatite (ap) components, and ellipses indicate convective mixing. Two open arrows in stage III indicate eruption through a ring fissure system.

chamber walls. Mixing between these magmas during reorganization mainly affects the trachyte magma which is also subject to further contamination in its marginal position. Intrusion of P1 basalt magma into the reservoir probably triggers the eruption, and all component magmas become intensely mixed during ascent to the surface.

Conclusions

The change from basaltic to silicic volcanism which occurred on Gran Canaria at around 14 Ma is also an important event in the evolution of other volcanic ocean islands but has not yet been studied in detail. The magmatic evolution of the composite flow P1, which formed during this transitional interval, involves changing mantle source composition, emplacement and sequential filling of separate magma reservoirs, differentiation by fractional crystallization, and variably efficient modifications by selective crustal contamination processes. This complex set of processes reflects the transient state of Gran Canaria's magmatic system caused by decreasing magma supply rates, formation of an intrusive core, and changing magma composition and eruptive behavior, which contrasts with the "steady state" conditions before and after this transition. Ongoing petrological and geophysical investigations are dedicated to the question of

what controls this important change in the evolution of a volcanic ocean island.

References

Akella, J., and F. R. Boyd, Partitioning of Ti and Al between coexisting silicates, oxides, and liquids. Proceedings of the Fourth Lunar Science Conference, Houston, Texas, *Geochim. Cosmochim. Acta, Suppl. 4,* 1049–1059, 1973.

Andersen, D. J., and D. H. Lindsley, New (and final!) models for the Ti-magnetite/ilmenite geothermometer and oxygen barometer, *Eos Trans. AGU, 66,* 416, 1985.

Bacon, C. R., Crystallization of accessory phases in magmas by local saturation adjacent to phenocrysts, *Geochim. Cosmochim. Acta, 53,* 1055–1066, 1989.

Bacon, C. R., and M. M. Hirschmann, Mg/Mn partitioning as a test for equilibrium between coexisting Fe-Ti oxides, *Am. Mineral., 73,* 57–61, 1988.

Banda, E., J. J. Dañobeitia, E. Suriñach, and J. Ansorge, Features

of crustal structure under the Canary Islands, *Earth Planet. Sci. Lett.*, *55*, 11–24, 1981.

Bishop, F. C., The distribution of Fe^{2+} and Mg between coexisting ilmenite and pyroxene with application to geothermometry, *Am. J. Sci.*, *280*, 46–77, 1980.

Blichert-Toft, J., C. E. Lesher, and M. T. Rosing, Selectively contaminated magmas of the Tertiary east Greenland macrodike complex, *Contrib. Mineral. Petrol.*, *110*, 154–172, 1992.

Blundy, J. D., and T. J. B. Holland, Calcic amphibole equilibria and a new amphibole-plagioclase geothermometer, *Contrib. Mineral. Petrol.*, *104*, 208–224, 1990.

Blundy, J. D., and T. J. B. Holland, Calcic amphibole equilibria and a new amphibole-plagioclase geothermometer: Reply to the comments of Hammarstrom and Zen, and Rutherford and Johnson, *Contrib. Mineral. Petrol.*, *111*, 269–272, 1992a.

Blundy, J. D., and T. J. B. Holland, Calcic amphibole equilibria and a new amphibole-plagioclase geothermometer—Reply to the comment of Poli and Schmidt, *Contrib. Mineral. Petrol.*, *111*, 278–282, 1992b.

Bogaard, P. v. d., H.-U. Schmincke, A. Freundt, C. M. Hall, and D. York, Eruption ages and magma supply rates during the Miocene evolution of Gran Canaria, *Naturwissenschaften*, *75*, 616–617, 1988.

Brey, G. P., and T. Köhler, Geothermobarometry in four-phase lherzolites, II, New thermobarometers, and practical assessment of existing thermobarometers, *J. Petrol.*, *31*, 1353–1378, 1990.

Brophy, J. G., Composition gaps, critical crystallinity, and fractional crystallization in orogenic (calc-alkaline) magmatic systems, *Contrib. Mineral. Petrol.*, *109*, 173–182, 1991.

Brown, W. L., Fractional crystallization and zoning in igneous feldspars: Ideal water-buffered liquid fractionation lines and feldspar zoning paths, *Contrib. Mineral. Petrol.*, *113*, 115–125, 1993.

Buddington, A. F., and D. H. Lindsley, Iron-titanium oxide minerals and synthetic equivalents, *J. Petrol.*, *5*, 310–357, 1964.

Bunsen, R., Über die Prozesse der vulkanischen Gesteinsbildungen Islands, *Ann. Phys. Chem.*, *83*, 197–272, 1851.

Cann, J. R., Bimodal distribution of rocks from volcanic islands, *Earth Planet. Sci. Lett.*, *4*, 479–481, 1968.

Chen, C. F., and J. S. Turner, Crystallization in a double-diffusive system, *J. Geophys. Res.*, *85*, 2573–2593, 1980.

Christensen, N. I., and G. H. Shaw, Elasticity of mafic rocks from the mid-Atlantic ridge, *Geophys. J. R. Astron. Soc.*, *20*, 271–284, 1970.

Clocchiatti, R., J. L. Joron, and M. Treuil, The role of selective alkali contamination in the evolution of recent historic lavas of Mt. Etna, *J. Volcanol. Geotherm. Res.*, *34*, 241–249, 1988.

Cousens, B. L., F. J. Spera, and G. R. Tilton, Isotopic patterns in silicic ignimbrites and lava flows of the Mogán and lower Fataga Formations, Gran Canaria, Canary Islands: Temporal changes in mantle source composition, *Earth Planet. Sci. Lett.*, *96*, 319–335, 1990.

Crisp, J. A., and F. J. Spera, Pyroclastic flows and lavas of the Mogán and Fataga formations, Tejeda volcano, Gran Canaria, Canary Islands: Mineral chemistry, intensive parameters, and magma chamber evolution, *Contrib. Mineral. Petrol.*, *96*, 503–518, 1987.

Daly, R. A., The geology of Ascension Island, *Proc. Am. Acad. Arts Sci.*, *60*, 1–180, 1925.

Donaldson, C. H., The rates of dissolution of olivine, plagioclase, and quartz in a basalt melt, *Mineral. Mag.*, *49*, 683–693, 1985.

Fisk, M. R., B. G. J. Upton, C. E. Ford, and W. M. White, Geochemical and experimental study of the genesis of magmas of Reunion Island, Indian Ocean, *J. Geophys. Res.*, *93*, 4933–4950, 1988.

Freundt, A., and H.-U. Schmincke, Mixing of rhyolite, trachyte and basalt magma erupted from a vertically and laterally zoned reservoir, Composite Flow P1, Gran Canaria, *Contrib. Mineral. Petrol.*, *112*, 1–19, 1992.

Giletti, B. J., Rb and Sr diffusion in alkali feldspars, with implications for cooling histories of rocks, *Geochim. Cosmochim. Acta*, *55*, 1331–1343, 1991.

Grove, T. L., and J. M. Donnelly-Nolan, The evolution of young silicic lavas at Medicine Lake Volcano, California: Implications for the origin of compositional gaps in calc-alkaline series lavas, *Contrib. Mineral. Petrol.*, *92*, 281–302, 1986.

Grove, T. L., M. B. Baker, and R. J. Kinzler, Coupled CaAl-NaSi

diffusion in plagioclase feldspar: Experiments and applications to cooling rate speedometry, *Geochim. Cosmochim. Acta*, *48*, 2113–2121, 1984.

Grove, T. L., R. J. Kinzler, and K. S. Bartels, Effects of pressure on alumina substitution in igneous augite: An empirical barometer, *Eos Trans. AGU*, *70*, 1401–1402, 1989.

Gudmundsson, A., Emplacement of dikes, sills and crustal magma chambers at divergent plate boundaries, *Tectonophysics*, *176*, 257–275, 1990.

Haggerty, S. E., Opaque mineral oxides in terrestrial igneous rocks, in *Oxide Minerals*, edited by D. Rumble III, *Mineral. Soc. Am. Short Course Notes*, *3*, 101–300, 1976.

Hammarstrom, J. M., and E.-A. Zen, Discussion of Blundy and Holland's (1990) "Calcic amphibole equilibria and a new amphibole-plagioclase geothermometer", *Contrib. Mineral. Petrol.*, *111*, 264–266, 1992.

Hanson, G. N., and C. H. Langmuir, Modelling of major elements in mantle-melt systems using trace element approaches, *Geochim. Cosmochim. Acta*, *42*, 725–741, 1978.

Harrison, T. M., and E. B. Watson, Kinetics of zircon dissolution and zirconium diffusion in granitic melts of variable water content, *Contrib. Mineral. Petrol.*, *84*, 66–72, 1983.

Harrison, T. M., and E. B. Watson, The behavior of apatite during crustal anatexis: Equilibrium and kinetic considerations, *Geochim. Cosmochim. Acta*, *48*, 1467–1477, 1984.

Helz, R. T., Phase relations of basalts in their melting ranges at $P_{H_2O} = 5$ kb, II, Melt compositions, *J. Petrol.*, *17*, 139–193, 1976.

Hinton, R. W., and B. G. J. Upton, The chemistry of zircon: Variations within and between large crystals from syenite and alkali basalt xenoliths, *Geochim. Cosmochim. Acta*, *55*, 3287–3302, 1991.

Hoernle, K. A., and H.-U. Schmincke, The petrology of the tholeiites through melilite nephelinites on Gran Canaria, Canary Islands: Crystal fractionation, accumulation and depths of melting, *J. Petrol.*, *34*, 573–597, 1993a.

Hoernle, K. A., and H.-U. Schmincke, The role of partial melting in the 15 Ma geochemical evolution of Gran Canaria: A blob model for the Canary hotspot, *J. Petrol.*, *34*, 599–626, 1993b.

Hoernle, K. A., G. Tilton, and H.-U. Schmincke, Sr-Nd-Pb isotopic evolution of Gran Canaria: Evidence for shallow enriched mantle beneath the Canary Islands, *Earth Planet. Sci. Lett.*, *106*, 44–63, 1991.

Hofmann, A. W., Diffusion in natural silicate melts: A critical review, in *Physics of magmatic processes*, edited by R. B. Hargraves, pp. 385–417, Princeton University Press, Princeton, N. J., 1980.

Holloway, J. R., and C. W. Burnham, Melting relations of basalt with equilibrium water pressure less than total pressure, *J. Petrol.*, *13*, 1–29, 1972.

Housh, T. B., and J. F. Luhr, Plagioclase-melt equilibria in hydrous systems, *Am. Mineral.*, *76*, 477–492, 1991.

Huppert, H. E., and R. S. J. Sparks, Melting the roof of a chamber containing a hot, turbulently convecting fluid, *J. Fluid Mech.*, *188*, 107–131, 1988a.

Huppert, H. E., and R. S. J. Sparks, The generation of granitic magmas by intrusion of basalt into continental crust, *J. Petrol.*, *29*, 599–624, 1988b.

Johnston, A. D., and P. J. Wyllie, Interaction of granitic and basic magmas: Experimental observations on contamination processes at 10 kbar with H_2O, *Contrib. Mineral. Petrol.*, *98*, 352–362, 1988.

Jones, W. B., Mixed benmoreite/trachyte flows from Kenya and their bearing on the Daly gap, *Geol. Mag.*, *116*, 487–489, 1979.

Koyaguchi, T., M. A. Hallworth, and H. E. Huppert, An experimental study on the effects of phenocrysts on convection in magmas, *J. Volcanol. Geotherm. Res.*, *55*, 15–32, 1993.

Langmuir, C. H., Geochemical consequences of in situ crystallization, *Nature*, *340*, 199–205, 1989.

Le Maitre, R. W., et al., *A Classification of Igneous Rocks and Glossary of Terms*, pp. 1–193, Blackwell Scientific, Boston, Mass., 1989.

Macdonald, R., R. S. J. Sparks, H. Sigurdsson, D. P. Mattey, D. W. McGarvie, and R. L. Smith, The 1875 eruption of Askja volcano, Iceland: Combined fractional crystallization and selective contamination in the generation of rhyolitic magma, *Mineral. Mag.*, *51*, 183–202, 1987.

Mahood, G. A., and A. N. Halliday, Generation of high-silica

rhyolite: A Nd, Sr, and O isotopic study of Sierra La Primavera, Mexican neovolcanic belt, *Contrib. Mineral. Petrol., 100,* 183–191, 1988.

Mahood, G. A., and W. Hildreth, Large partition coefficients for trace elements in high-silica rhyolites, *Geochim. Cosmochim. Acta, 47,* 11–30, 1983.

Marsh, B. D., B. Gunnarsson, R. Congdon, and R. Carmody, Hawaiian basalt and Icelandic rhyolite: Indicators of differentiation and partial melting, *Geol. Rundsch., 80,* 481–510, 1991.

McBirney, A. R., Mixing and unmixing of magmas, *J. Volcanol. Geotherm. Res., 7,* 357–371, 1980.

McBirney, A. R., B. H. Baker, and R. H. Nilson, Liquid fractionation, I, Basic principles and experimental simulations, *J. Volcanol. Geotherm. Res., 24,* 1–24, 1985.

Myers, J. D., and B. D. Marsh, Geology and petrogenesis of the Edgecumbe volcanic field, SE Alaska: The interaction of basalt and sialic crust, *Contrib. Mineral. Petrol., 77,* 272–287, 1981.

Naney, M. T., Phase equilibria of rock-forming ferromagnesian silicates in granitic systems, *Am. J. Sci., 283,* 993–1033, 1983.

Nielsen, R. L., and M. J. Drake, Pyroxene-melt equilibria, *Geochim. Cosmochim. Acta, 43,* 1259–1272, 1979.

Nockolds, S. R., The idea of contrasted differentiation: A reply, *Geol. Mag., 73,* 529–535, 1936.

Patchett, P. J., Thermal effects of basalt on continental crust and crustal contamination of magmas, *Nature, 283,* 559–561, 1980.

Poli, S., and M. W. Schmidt, A comment on "Calcic amphibole equilibria and a new amphibole-plagioclase geothermometer" by J. D. Blundy and T. J. B. Holland (Contrib. Mineral. Petrol. (1990) 104: 208–224), *Contrib. Mineral. Petrol., 111,* 273–278, 1992.

Rutherford, M. J., and M. C. Johnson, Comment on Blundy and Holland's (1990) "Calcic amphibole equilibria and a new amphibole-plagioclase geothermometer," *Contrib. Mineral. Petrol., 111,* 266–268, 1992.

Ryan, M. P., Neutral buoyancy and the mechanical evolution of magmatic systems, in Magmatic Processes: Physicochemical Principles, edited by B. O. Mysen, *Geochem. Soc. Spec. Publ., 1,* 259–287, 1987.

Schmincke, H.-U., Cone sheet swarm, resurgence of Tejeda caldera, and the early geologic history of Gran Canaria, *Bull. Volcanol., 31,* 153–162, 1967.

Schmincke, H.-U., Ignimbrite sequence on Gran Canaria, *Bull. Volcanol., 33,* 1199–1219, 1969a.

Schmincke, H.-U., Petrologie der phonolithischen bis rhyolithischen Vulkanite auf Gran Canaria, Kanarische Inseln, habilitation thesis, Univ. of Heidelberg, Germany, 1969b.

Schmincke, H.-U., The geology of the Canary Islands, in *Biogeography and Ecology in the Canary Islands,* edited by G. Kunkel, pp. 67–184, The Hague, Netherlands, 1976.

Schmincke, H.-U., Volcanic and chemical evolution of the Canary Islands, in *Geology of the Northwest African Continental Margin,* edited by U. von Rad, K. Hinz, M. Sarnthein, and E. Seibold, pp. 273–306, Springer-Verlag, New York, 1982.

Schmincke, H.-U., with contributions by A. Freundt, H. Ferriz, G. Kobberger, and P. Leat, *Geological Field Guide to Gran Canaria,* Pluto, Witten, Germany, 1990.

Shaw, H. R., Links between magma-tectonic rate balances, plu-tonism, and volcanism, *J. Geophys. Res., 90,* 11,275–11,288, 1985.

Sparks, R. S. J., H. E. Huppert, and J. S. Turner, The fluid dynamics of evolving magma chambers, *Philos. Trans. R. Soc. London A, 310,* 511–534, 1984.

Spencer, K. J., and D. H. Lindsley, A solution model for coexisting iron-titanium oxides, *Am. Mineral., 66,* 1189–1201, 1981.

Spulber, S. D., and M. J. Rutherford, The origin of rhyolite and plagiogranite in oceanic crust: An experimental study, *J. Petrol., 24,* 1–25, 1983.

Stern, C. R., W. L. Huang, and P. J. Wyllie, Basalt-andesite-rhyolite-H_2O: Crystallization intervals with excess H_2O and H_2O-undersaturated liquidus surfaces to 35 kilobars, with implications for magma genesis, *Earth Planet. Sci. Lett., 28,* 189–196, 1975.

Stormer, J. C., The effects of recalculation on the estimates of temperature and oxygen fugacity from analyses of multicomponent iron-titanium oxides, *Am. Mineral., 68,* 586–594, 1983.

Tait, S. R., G. Wörner, P. v. d. Bogaard, and H.-U Schmincke, Cumulate nodules as evidence for convective fractionation in a phonolite magma chamber, *J. Volcanol. Geotherm. Res., 37,* 21–37, 1989.

Tsuchiyama, A., Dissolution kinetics of plagioclase in the melt of the system diopside-albite-anorthite, and origin of dusty plagioclase in andesites, *Contrib. Mineral. Petrol., 89,* 1–16, 1985.

Watson, E. B., Diffusion in magmas at depth in the Earth: The effect of pressure and dissolved H_2O, *Earth Planet. Sci. Lett., 52,* 291–301, 1981.

Watson, E. B., and C. J. Capobianco, Phosphorous and the rare earth elements in felsic magmas: An assessment of the role of apatite, *Geochim. Cosmochim. Acta, 45,* 2349–2358, 1981.

Watson, E. B., and T. M. Harrison, Zircon saturation revisited: Temperature and composition effects in a variety of crustal magma types, *Earth Planet. Sci. Lett., 64,* 295–304, 1983.

Watson, E. B., and S. R. Jurewicz, Behavior of alkalies during diffusive interaction of granitic xenoliths with basaltic magma, *J. Geol., 92,* 121–131, 1984.

Wones, D. R., Biotites and amphiboles in igneous rocks: Dehydration redox reactions, in *Amphiboles: Petrology and Experimental Phase Relations, Rev. Mineral.,* vol. 9B, edited by V. R. Veblen and P. H. Ribbe, pp. 357–371, American Mineralogical Society, Washington, D. C., 1982.

Wood, D. A., A variably veined suboceanic upper mantle—Genetic significance for mid-ocean ridge basalts from geochemical evidence, *Geology, 7,* 499–503, 1979.

Wyllie, P. J., Effects of changes in slope occurring on the liquidus and solidus paths in the system diopside-anorthite-albite, *Mineral. Soc. Am. Spec. Pap., 1,* 204–212, 1963.

Wyllie, P. J., Petrogenesis and the physics of the Earth, in *The Evolution of the Igneous Rocks,* edited by H. S. Yoder, pp. 483–520, Princeton University Press, Princeton, N. J., 1979.

A. Freundt and H.-U. Schmincke, GEOMAR, Forschungszentrum für marine Geowissenschaften, Abteilung Vulkanologie und Petrologie, Wischhofstr. 1-3, D-24148 Kiel, Germany.